Positron Emission Tomography to Evaluate Cardiac Remodelling After Collagen Hydrogel Therapy

Mary MacMullin

Thesis submitted to the University of Ottawa in partial fulfillment of the requirements for the Master of Applied Science - Biomedical Engineering

Faculty of Engineering
University of Ottawa

Abstract

Despite the development of therapeutic interventions to prevent mortality following myocardial infarction (MI), there is a significant long-term risk of developing heart failure (HF). Injectable collagen hydrogels have demonstrated considerable promise as a therapeutic solution to reduce adverse ventricle remodeling associated with the development of HF post-MI. Matrix metalloproteinases (MMPs) are proteolytic enzymes involved in the degradation of the structural components of the extracellular matrix (ECM). The activation of MMPs following MI is an essential step in the cardiac repair process. However, uncontrolled enzymatic activity during this time has been associated with the formation of adverse fibrosis. Given the role of the proteases in tissue remodeling, MMPs may be a potential biomarker to predict the development of HF.

This thesis work seeks to examine the effect of a novel hydrogel matrix therapy on cardiac tissue post-MI using broad-spectrum MMP-targeted radiotracer, [^{18}F]BR3531. In Study 1, serial positron emission tomography (PET) imaging was performed to elucidate the spatial and temporal binding of [^{18}F]BR351 post-MI using a murine model. Imaging was performed by administering [^{18}F]BR351 at time points corresponding with periods of peak MMP activation post-MI. *In vivo* PET imaging and *in vitro* autoradiography demonstrated decreased [^{18}F]BR351 binding in the infarct region. In Study 2, the model was used to evaluate the efficacy of a therapeutic collagen hydrogel to attenuate tissue remodeling. The groups that received the matrix treatment exhibited improved [^{18}F]BR351 uptake in the infarct region. However, conflicting results between *in vivo* imaging and *in vitro* autoradiography, and immunohistochemistry using MMP2 and MMP9 indicate that [^{18}F]BR351 may not be suited for MMP imaging in mouse models of MI.

Table of Contents

List of Abbreviations

AT – Attenuation Correction

CVD – Cardiovascular Disease

CT – Computed Tomography

ECM – Extracellular Matrix

EMB – Endomyocardial Biopsy

FBS – Fetal Bovine Serum

HF – Heart Failure

HLA – Horizontal Long Axis

IHC – Immunohistochemistry

IAW – Inveon Acquisition Workplace

IC_{50} – Half-Maximal Inhibitory Concentration

LAD – Left Anterior Descending

LV – Left Ventricle

LVEF – Left Ventricular Ejection Fraction

MRI – Magnetic Resonance Imaging

MMP – Matrix Metalloproteinase

MMPI – Matrix Metalloproteinase Inhibitor

MI – Myocardial Infarction

OCT – Optimal Cutting Temperature

PFA – Paraformaldehyde

PLA – Parasternal Long Axis

PBS – Phosphate Buffered Saline

PCR – Polymerase Chain Reaction

PET – Positron Emission Tomography

ROI – Region of Interest

RLU – Relative Light Units

SA – Short Axis

SPECT – Single Photon Emission Computed Tomography

SNR – Signal to Noise Ratio

SE – Standard Error

TAC – Time Activity Curve

TIMP – Tissue Inhibitor of Metalloproteinase

VLA – Vertical Long Axis

List of Figures

Acknowledgements

First and foremost, I would like to express my sincere gratitude to my supervisor, Dr. Erik Suuronen, for allowing me to be a part of his lab. A heartfelt thank you for your patience, support, and feedback.

A special thanks to the members of the Suuronen Lab. I would like to thank Dr. Veronika Sedlakova, Dr. Ines Amara, Dr. Cagla Eren Cimenci, Madison Bak, and Eva Sheppard-Perkins. I am grateful to have found an incredible group of mentors, role models, and friends. A special thanks to Cagla – it has been a privilege to learn from you.

Also, I would like to express my gratitude to Dr. Benjamin Rotstein for his guidance, and the members of the Rotstein lab, including Dr. Maxime Munch and Ariel Buchler, who were essential to the completion of this project. In addition, I would like to thank Dr. Robert deKemp for his guidance in imaging analysis.

Finally, I would like to thank my friends and family for their endless love and unwavering support.

1. Introduction

1.1. Myocardial Infarction

Myocardial infarction (MI) is a clinical phenomenon characterized by the abrupt cessation of blood flow to one or more regions of the myocardium due to the occlusion of one or more coronary arteries. MI frequently occurs as a result of underlying coronary artery disease due to atherosclerosis (Ojha et al., 2021). The narrowing and subsequent blockage of the artery is a result of atherosclerosis, whereby the formation and rupture of dense cholesterol and lipid-rich plaques in the coronary artery results in a rapid inflow of thrombogenic lipids and activation of platelets and clotting factors leading to the acute ischemic event (Badimon et al., 2012; Linton et al., 2000). Approximately 70 percent of MI events are attributed to coronary atherosclerosis (Mechanic et al., 2022); other possible causes of MI may include trauma, congenital coronary abnormalities, and embolism (Saleh & Ambrose, 2018). Due to a lack of oxygen supply, the myocardium suffers serious injury, leading to necrosis of the cardiac tissue (Chiong et al., 2011).

Since the 1970s, the on-going development of sensitive diagnostic techniques, rapid intervention, and improved management has drastically reduced the mortality due to acute MI (Boateng & Sanborn, 2013). Revascularization techniques such as percutaneous intervention (PCI) and antithrombotic therapy have greatly reduced the incidence of death immediately following injury (Thiene & Basso, 2010). Although early intervention may assist in preserving the myocardium, there remains a considerable latent risk of developing heart failure (HF) (Boateng & Sanborn, 2013). For patients with late presentation (12 hour to 24 hours after onset of symptoms), the therapeutic benefit of revascularization is limited due to irreversible myocardial loss after coronary occlusion (Dauerman & Ibanez, 2021). However, evidence

suggests partial myocardial salvage indicating a stratified approach to treatment may be valuable to ensure maximum preservation of the cardiac tissue (Hugenholtz et al., 1986).

The underlying cause of HF secondary to MI is attributed to altered structural properties of the left ventricle (LV) due to post-infarction remodeling. During the innate healing process, the infarct region is replaced with a collagenous scar tissue (Murtha et al., 2017). Due to the altered structural and mechanical properties of the scar tissue, compensatory mechanisms are activated (Bhatt et al., 2017). Unfortunately, the modified cardiac function is unsustainable, and unable to meet metabolic demands long-term, leading to the development of HF. It is noted that there currently lacks a universally accepted clinical definition of HF; however, it is recognized that its development is vital to promoting standardization of care (Bozkurt et al., 2021). Seeking to develop a universal definition and classification of HF, a consensus statement was published from global cardiovascular associations which defined HF as the structural and/or functional cardiac abnormalities, with evidence of biomarker evidence of HF, and consideration of left ventricular ejection fraction (LVEF) (Abramov & Kittleson, 2021; Bozkurt et al., 2021) .

1.2. Cardiac Repair and Remodeling

Following MI, a robust wound-healing process is initiated, referred to as post-infarction LV remodeling (van der Bijl et al., 2020). The remodeling process is broadly characterized by a variety of physiological changes, including cardiomyocyte death, hypertrophy of surviving cardiomyocytes, a robust inflammatory reaction, and formation of a dense, collagenous scar (Farache Trajano & Smart, 2021; Hsieh et al., 2007; Mezzaroma et al., 2011). Successful wound healing is indicated by the ability of the reformed tissue to maintain ventricle geometry and cardiac function (Mouton et al., 2018). The extent of cardiac remodeling exhibited in the

infarcted and non-infarcted myocardium following MI is a major determinant of survival after acute MI, and a predictor for the likelihood of developing HF (st. John Sutton & Sharpe, 2000). The reparative process initiated following the MI event occurs in three discrete, but overlapping phases: the inflammatory phase, the proliferation phase, and the maturation phase (Murtha et al., 2017).

1.2.1. The Inflammatory Phase

The initial inflammatory stage is the early response to the MI event. Due to the coronary artery obstruction, the blood supply to the myocardium is discontinued. As a result, the amount of oxygen available for consumption is diminished, causing cardiomyocytes to enter a state of hypoxia (Chiong et al., 2011). Approximately 3 hours after the onset of ischemia, cardiomyocytes begin to undergo cell death via apoptosis, necrosis, and autophagy, initiating a robust inflammatory response (Chiong et al., 2011; Jenča et al., 2021). Chemokine signalling promotes the recruitment of inflammatory cells, including neutrophils, macrophages, and lymphocytes to the injured region and surrounding area (Richardson et al., 2015) The infiltration of inflammatory cells into the infarct and border regions is further facilitated by increased vessel permeability due to endothelial activation (Nian et al., 2004). During the inflammatory phase, inflammatory cells begin to secrete and activate endogenous matrix metalloproteinases (MMPs). The activation of MMPs initiates the progressive degradation and resorption of the injured extracellular matrix (ECM) and necrotic cells (Ertl & Frantz, 2005). The removal of the substrates obtained from the breakdown of the original ventricle structure by leukocytes facilitates the deposition of new structural components (Ertl & Frantz, 2005). Concurrently, an upregulation of matrix proteins and glycosaminoglycans results in deposition of a provisional

granulation tissue. The preliminary ECM, which is comprised of fibrin, laminin, fibronectin and proteoglycans, creates a temporary structural network that is vital to preventing ventricular rupture post-MI (Richardson et al., 2015). In addition, the provisional matrix tissue creates a favourable environment to facilitate the infiltration, migration, and proliferation of key cell types and structural integrity pending the formation of the secondary matrix (Barker & Engler, 2017). The concentration of matrix molecules remains elevated for the remainder of the inflammatory period until the proliferative phase during which fibrillar collagen is deposited to form the cardiac scar tissue (Richardson et al., 2015).

The inflammatory phase is initiated within minutes to hours following the MI event. In mice, the duration of the inflammatory phase occurs between 1 and 48 hours after injury, and between 1 hour to 4 days in large animals and humans (Christia et al., 2013; Prabhu & Frangogiannis, 2016). Upon exerting the appropriate inflammatory response, there is a transition to the proliferative stage. The progressive decrease in cardiac expression of inflammatory cytokines and apoptosis of inflammatory cells indicates the conclusion of the inflammatory phase.

1.2.2. The Proliferative Phase

The expression of inflammatory cells decreases as a variety of inhibitory pathways, collectively referred to as 'stop signals', are activated; macrophages secrete anti-inflammatory cytokines to initiate the decline of the vigorous inflammatory response (Christia & Frangogiannis, 2013). The ensuing proliferative phase is characterized by the formation of neovessels, myofibroblast transdifferentation, and the deposition of ECM components (Prabhu & Frangogiannis, 2016).

The proliferative phase is dominated by the actions of the myofibroblasts. A high concentration of myofibroblasts is achieved by the migration, proliferation, and differentiation of cardiac fibroblasts into activated myofibroblasts (Gibb et al., 2020). This phenomenon is supported by the secretion of growth factors from macrophages to promote the recruitment and activation of myofibroblasts (Little et al., 2020). The increased number of myofibroblasts persists for several weeks post-injury.

The myofibroblast expression of pro-collagen drastically increases, peaking at approximately 1-week after injury and remains elevated for several weeks to months before returning to baseline (Richardson et al., 2015). The deposition of collagen is regulated by the activation of MMP and tissue inhibitors of metalloproteinases (TIMPs). In addition to the deposition of collagen, matricellular protein are also expressed in the myocardium. The deposition of matricellular proteins in the border zone helps to inhibit remodeling of the border zone and remote myocardium (Frangogiannis, 2012; Matsui et al., 2010).The deposition of matricellular proteins occurs in a migratory motion towards the core infarct region along the newly synthesized ECM (Matsui et al., 2010).

It is estimated that the proliferative phase activity occurs 2 to 7 days following MI followed by transient plateau of collagen production in small animals (Christia et al., 2013; Prabhu & Frangogiannis, 2016; Richardson et al., 2015; Yang et al., 2002). In humans, the proliferation phase of healing may occur between 4 and 14 days following MI (Christia et al., 2013; Yang et al., 2002).

1.2.3. The Maturation Phase

In the final maturation phase, fibroblasts undergo apoptosis, neovessels formed during the proliferative phase regress from the infarct region, and the newly formed collagenous matrix matures by condensation into a mature scar (Bonaventura et al., 2016).

During the maturation stage, ongoing replacement of collagen type III by collagen type I by myofibroblasts initiated at the end of the proliferative phase reaches an end as collagen content begins to stabilize and mature via cross-linking (French & Kramer, 2007). Following the deposition of type I collagen, the protein undergoes a condensation reaction due to the upregulation of lys-oxidase (LOX) catalysis during which the enzyme lysyl oxidase, the cross-linkers hydroxlysylpyridinium and hydroxylysylpyridinoline, and proteoglycans bind to collagen and regulate fibrillogenesis and fiber diameter (el Hajj et al., 2018). The extent of cross-linking determines the material properties of the scar tissue, including solubility, stiffness, and resistance to degradation of the resulting fibrils (Fratzl & Weinkamer, 2007). A prolonged time to condensation of collagen creates a susceptibility for infarct expansion due to insufficient structural support; however, excessive scar formation may result in non-ischemic infarct extension (Pytliak et al., 2017).

At this time, angiogenic cells undergo apoptosis, resulting in the dissolution of the microvascular network previously established in the infarct region (Talman & Ruskoaho, 2016). The loss of blood supply halts the supply of cell signals and growth factors. Concurrently, myofibroblasts undergo apoptosis, stopping the deposition of collagen in the infarct region (Klingberg et al., 2013). Although the number of myofibroblasts in the infarct region is decreased, a moderate population remains present (Richardson et al., 2015). The result of the extensive post-MI healing process is a mature, fibrous collagen scar tissue.

The length of the maturation phase varies. The remodeling in the intact region may be resolved relatively quickly, however altered regional stress caused by the modified mechanical properties of the infarct zone, may lead to ongoing maladaptive remodeling of the border zone and remote region for an extended period of time. The maturation phase occurs between 7 to 28 days, and 14 days to 2 months for mice and humans, respectively (Richardson et al., 2015).

1.2.4. Ventricular Remodeling and the Pathophysiology of Heart Failure

The adaptive mechanism of left ventricular remodeling involving the marked increase in deposition and cross-linking of collagens type I and III may lead to HF after MI (Soufen et al., 2008). Infarct size is reportedly the greatest predictor of ventricular remodeling; collectively, the size, location, composition, and mechanical properties of the formed scar tissue are predictors of patient outcome post-MI (Richardson et al., 2015; Wu et al., 2008). Due to the morphological and histological changes associated with the fibrotic response in the infarct region after MI that are unlike the properties of healthy myocardium tissue, the heart exhibits altered mechanosensing, decreased contractility, impaired elasticity and diastolic dysfunction (Schirone et al., 2017). To accommodate for an increased mechanical stress burden on the infarct region and to ensure a sufficient ejection fraction is achieved, regional load bearing on the border zone and healthy region of the myocardium is increased (Burchfield et al., 2013). Attempting to sustain long-term compensatory cardiac function results in scar enlargement, ventricle dilatation, and geometrical changes in the ventricle (st. John Sutton & Sharpe, 2000). The progression of ventricular remodeling and decreased functional capacity prevent the metabolic demands of the heart from being met, indicating the onset of HF.

1.3. The Cardiac Extracellular Matrix

The cardiac ECM is a dynamic, complex three-dimensional network vital to the structural integrity required to maintain the shape and geometry of the left LV. Additionally, the scaffold creates a suitable environment to support native cell types and extracellular molecules (Chan & Leong, 2008). The ECM is comprised of a variety of macromolecules, such as structural proteins, signaling molecules, and proteases. In addition, the cardiac ECM contains non-structural extracellular macromolecules, such as glycosaminoglycans, proteoglycans, and glycoproteins that assist in regulating the ECM properties (Frangogiannis, 2019).

The structural integrity and tensile strength of the cardiac ECM is due to an abundance of fibrillar collagen types I and III organized into complex fibrils and networks (Jugdutt, n.d.). The collagenous network is produced by cardiac fibroblasts (Souders et al., 2009). The relative amount of the fibrillar protein subtypes determines the mechanical properties of the myocardium. Type I collagen constitutes the majority (85%) of the ECM network (Horn & Trafford, 2016) and provides the tensile strength (Xue & Jackson, 2015). Collagen type III (11%) is a thin fibrillar protein and provides the elastic properties (Kuivaniemi & Tromp, 2019). Additionally, lesser amounts of collagen types IV, V, VI, and VIII are present in the myocardium (Li et al., 2018). Other structural proteins, such as elastin and fibronectin, are also present in the heart (Rienks et al., 2014).

The triple helix conformation of collagen is resistant to the action of many proteases, but susceptible to degradation by the action of enzyme capthesin K and collagenolytic matrix metalloproteinase (MMPs) enzymes (Laronha & Caldeira, 2020). Following denaturation, collagen is referred to as gelatin, which can be further reduced by gelatinases (Diegelmann, 2004). The degradation of collagen is essential to a variety of biological processes, including

embryogenesis, morphogenetic, tissue demodulation, angiogenesis, and wound healing (Mathew-Steiner et al., 2021). The regulation of ECM homeostasis via collagen synthesis and degradation is achieved by the action of MMPs and its inhibitors, the tissue inhibitors of metalloproteinases (TIMPs).

1.4. Matrix Metalloproteinases

MMPs are a family of calcium and zinc-dependent proteolytic enzymes involved in the regulation of the ECM and inflammatory signaling. A total of 28 MMPs have been identified, however only 24 MMPs have been found in human tissue (Cui et al., 2017). The general structure of MMPs consists of 4 components: a propeptide sequence, a catalytic domain, a hinge region or linker protein, and a hemopexin domain (Nagase et al., 2006). The hemopexin domain largely determines the collagen substrate specificity, thus implicated in the classification of MMPs (Deleon-Pennell et al., 2016; Laronha & Caldeira, 2020). MMPs were previously categorized according to the substrate it was initially observed to cleave, however, it was later determined that MMPs may cleave multiple substrates, thus the classification system has been refined with reference to substrate specificity, sequential similarity, and domain organization: collagenase, gelatinase, stromelysins, matrilysins, membrane-type MMPs, and non-classified MMPs (Lindsey et al., 2016).

MMPs regulate the ECM by maintaining a balance of collagen synthesis and degradation. These proteases can degrade collagens I, II, III, IV, V, VI, VII, VIII, IX, X, and XIV with varying efficacies, in addition to non-collagen ECM substrates, such as aggrecan, entactin, fibronectin, tenascin, laminin, myelin basic protein, and vitronectin (Cui et al., 2017; Ma et al., 2020). MMPs are typically released in the form of inactive zymogens, or pro-enzymes (pro-

MMPs). To degrade its substrate, MMPs must be activated via cleavage of the cysteine switch by proteolytic enzymes, causing the pro-domain to detach (Hadler-Olsen et al., 2011). Following activation, the catalytic domain interacts with the target protein at a designated site, resulting in the modification – or degradation – of the target biological molecule (Costa, 2016). However, it is noted that select MMPs, such as MMP9, are capable of exhibiting enzymatic activity in its pro-MMP form without undergoing cleavage (Ra & Parks, 2007). The cleavage of ECM components by the associated MMP-types results in the production of substrate fragments, or matricryptins (Frangogiannis & Kovacic, 2020). The production of select matricryptins have been identified as producing a bioactive effect, thus have also been investigated for their biological role in post-MI tissue (Frangogiannis & Kovacic, 2020).

In addition to degrading the ECM and its components, MMPs are also involved in the inflammatory response and cell signaling. The proteases assist in regulating of non-matrix molecules, such as growth factors, inflammatory factors, and integrins, thus are involved in a variety of normal physiological processes, including cell proliferation, migration, differentiation, cell apoptosis, angiogenesis, wound repair, and immunity (Q. Chen et al., 2013). Given MMPs are fundamental to a variety of biological processes, strict regulation of their expression is required to prevent deleterious effects.

Physiological MMP activity is regulated via a variety of pathways including mRNA expression, proenzymatic activation, and inhibition by local endogenous tissue inhibitors of metalloproteinases (TIMPs) (Creemers et al., 2001). In addition to regulation of MMP activity, TIMPs can elicit independent biological actions (Brew & Nagase, 2010). The ratio of MMP/TIMP is critical to maintaining normal biological function.

1.4.1. The Role of MMPs in Post-MI Repair

Following MI, a variety of MMP subtypes are secreted by various native and infiltrating cell types, including neutrophils, macrophage, endothelial cells, myocytes, and fibroblasts (Lambert et al., 2008). The expression of MMP1, MMP2, MMP3, MMP8, MMP9, MMP13, MMP12, MMP28, and MMPs MT1-MMP, and all 4 TIMPs have been identified in the myocardium post-MI (Lindsey, 2018; Matrisian, 1990). The activation of MMP enables the removal of necrotic cardiac ECM, thereby enabling the deposition of a new provisional ECM. However, uncontrolled MMP activation has been identified as a prognostic marker in the development of HF. Whereas normal physiological conditions indicate a relatively low basal level of MMP activity, pathological remodeling can demonstrate an accelerated ECM turnover rate – approximately 5 to 10-fold during MI (el Hajj et al., 2018). Excessive protease activity results in collagen degradation, deterioration of connective tissue, impaired myocardial integrity, and ventricular remodeling (Brower et al., 2006).

The activation of MMPs exerts a vital function in the post-MI response. The degree of left ventricular remodeling may be influenced by the temporal activation pattern of MMPs. Prolonged, uncontrolled MMP activation and insufficient TIMP levels increases the likelihood of developing chronic, adverse fibrosis (Raeeszadeh-Sarmazdeh et al., 2020). Previous research concerning the use of MMP inhibitor agents have demonstrated benefit when suppressing MMP activity post-MI. However, excessive inhibition of MMP is associated with advanced fibrosis (Liu et al., 2006). This is attributed to the excess of TIMP relative to MMPs, resulting in an excessively fibrotic condition (Arpino et al., 2015; Liu et al., 2006). A greater understanding of the temporal activation of MMPs will assist in establishing treatment timepoints to achieve the greatest therapeutic benefit.

The stages of wound healing correlate to distinct spatial and temporal activation of various MMP types (Fig. 1). In mice and rats, the activation of MMPs typically occurs within 24 hours of the MI event, achieves peak concentration between 5 to 7 days, and remains elevated between 7- and 14-days post-MI, which is followed by a transient decrease in MMP activation as TIMP expression increases (DeLeon-Pennell et al., 2017; Phatharajaree et al., 2007). However, the precise pattern of MMP activation is specific to the region of the myocardium and MMP type. The roles of gelatinases MMP2 and MMP9 in post-MI remodelling have been substantially investigated. The substrates targeted by these gelatinases include gelatin, collagen types 4,5,8,10,11, and 14, elastin, proteoglycan core proteins, fibronectin, laminins, fibrilin-1,TNF-alpha and IL-1b (Laronha & Caldeira, 2020). Additionally, MMP2 and MMP9 may also behave as collagenases, however the former exhibits collagenase degradation to a lesser extent (Cui et al., 2017). In a murine model, MMP-2 activation occurs within 4 days post-MI with peak activity noted at day 7 before exhibiting a return to basal levels beginning on day 14 (Iyer et al., 2014; Tao et al., 2004). Given that MMP-2 is continually detected in the myocardium, it is considered a housekeeping gene involved in normal physiological ECM turnover. Similarly, circulating MMP-9 is detected within 1-day post-MI and peaks at day 7 (DeLeon-Pennell et al., 2014).The role of gelatinase activation in adverse remodeling and structural modifications has led to its implication as a prognostic biomarker for HF.

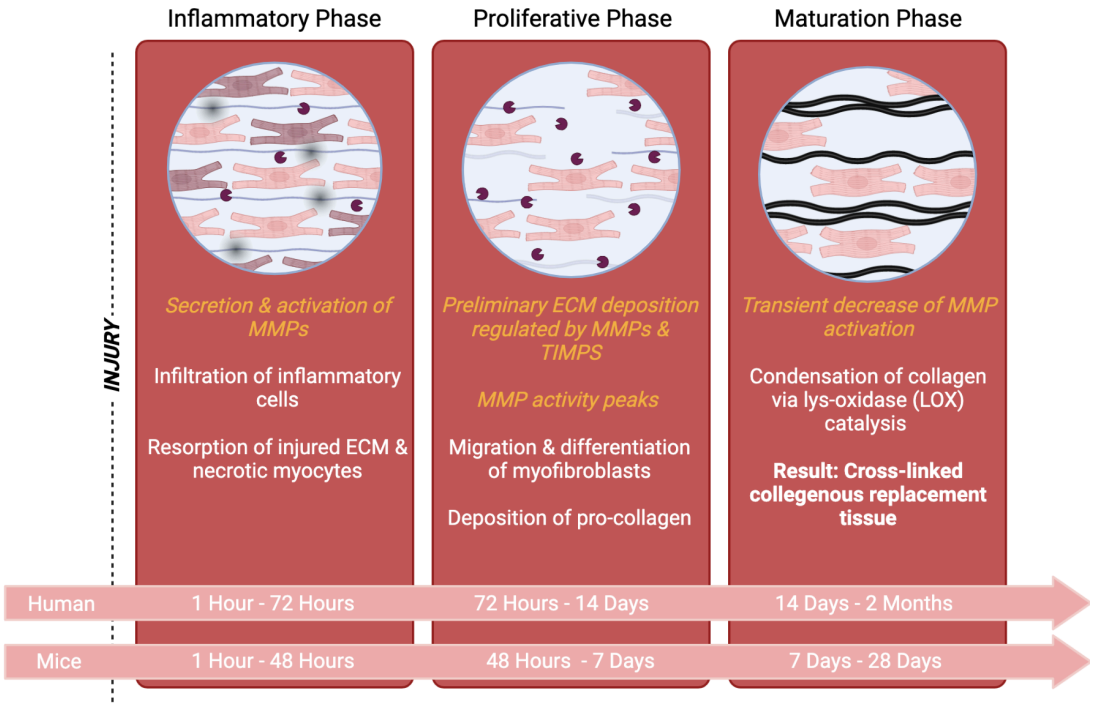

Figure 1. Overview of MMP activity during the cardiac repair cycle. The pattern of activation of MMPs can be correlated to the three stages of the cardiac repair process: inflammatory, proliferative, and maturation phase of the reparative process. Within hours of the acute ischemic event, the heart enters the inflammatory phase. The infiltrating inflammatory cells begin secreting and activating MMPs. During this time, MMPs begin to degrade the necrotic or injured ECM to enable infiltration of new, healthy cells. In the proliferative phase, the migration and differentiation of myofibroblasts produce pro-collagen. The deposition of preliminary components is regulated by MMPs and endogenous TIMPS. During the maturation phase, MMP activity decreases and pro-collagen undergoes condensation LOX catalysis to form a highly crosslinked replacement tissue. Made with BioRender©.

1.5. Biomaterials and Tissue Regeneration

Following survival of the acute ischemic event, the risk of post-infarct HF becomes an area of concern. Various medical and surgical interventions, such as coronary stent insertion, angioplasty, or heart transplant, may be required to manage or treat the symptoms of HF, however, they do not address underlying post-ischemic remodeling (di Franco et al., 2018). Given the heart's limited self-renewal and regenerative ability, a new therapeutic approach to

restore functional tissue is needed. The emergence of tissue engineering and biomaterials has enabled the development of novel treatments important to regenerative medicine. The optimal therapy is idealized to be able to minimize myocardial death, optimize cardiac repair, and reduce adverse cardiac remodeling (Vilahur et al., 2011). Numerous new treatment strategies for targeting the ischemic remodeling are undergoing evaluation; however, they have not yet completed clinical trials, and there remains a need for a disease-modifying therapy (Contessotto & Pandit, 2021). Nonetheless, positive results support the potential of biomaterials as a treatment to ameliorate the adverse cardiac remodeling and reduce the probability of developing chronic HF.

A novel collagen hydrogel has been developed by the Cardiovascular Tissue Engineering Laboratory at the University of Ottawa Heart Institute to reduce the adverse cardiac remodeling has undergone extensive investigation (Ahmadi et al., 2015; Blackburn et al., 2015; McLaughlin et al., 2019; Pupkaite et al., 2020). The collagen hydrogels are polymer networks that are formed using chemical cross-linkers enabling their solidification upon exposure to body temperature. The administration of a hydrogel provides a scaffold for the infiltration, migration and proliferation of essential molecular signals, growth factors, and cells (El-Sherbiny & Yacoub, 2013). Furthermore, the collagen matrices demonstrate considerable biocompatibility and bioactivity (Khan & Khan, 2013). Previous evidence has demonstrated that when administered to the infarct region post-MI, collagen scaffolds have the potential to reduce adverse remodeling and limit cardiac dysfunction by modulating the inflammatory response, promoting angiogenesis, and decreasing fibrosis (Blackburn et al., 2015; McLaughlin et al., 2019). Additionally, the structure of hydrogels behave as an excellent vehicle for the delivery of

cell types, growth factors, and other therapeutic agents, which has further contributed to its therapeutic benefit.

A variety of assessments seeking to optimize the efficacy of the collagen hydrogel have been performed. A previous investigation using rat tail type I collagen to determine the effect of early versus delayed administration of biomaterial, the former exhibiting the greatest therapeutic benefit was during the early inflammatory phase after the MI event (Blackburn et al., 2015). Research concerning the efficacy of collagen hydrogels using human recombinant collagen hydrogels have previously demonstrated a beneficial effect post-MI response following the delayed administration of the material (delivery at 1-week post-MI) (McLaughlin et al., 2019). Furthermore, evidence of a therapeutic effect for late administration of the material supports its use in patients who are unable to receive early intervention due to delayed diagnosis or inaccessible to treatment. Ongoing investigation of the mechanisms of the collagen hydrogel will provide greater understanding necessary to support its translation into clinical practice.

1.6. Extracellular Matrix Imaging Techniques

Endomyocardial biopsy (EMB) is the current gold standard for the detecting cellular-level changes in the cardiac ECM (Karamitsos et al., 2020). Samples obtained from EMB are subsequently processed for light microscopy examination using hematoxylin and eosin staining to evaluate gross morphology; and Massons, movat or elastic trichrome, or picrosirius red staining to examine collagen and elastic tissue for calculating the myocardial collagen volume fraction (Arteaga et al., 2009; Cooper et al., 2007; Hahn et al., 2020). Other analyses of EMB samples may include molecular studies, immunofluorescence or immunohistochemistry, and polymerase chain reaction (PCR) (Cooper et al., 2007). However, given the invasiveness of

EMB, its use is largely limited to patients for monitoring transplant rejection status, unexplained cardiomyopathies, cardiac tumours, and anthracycline-induced cardiomyopathies, unexplained arrythmias, and cardiac tumours (Cooper et al., 2007; From et al., 2011). For patients that do not fit the criteria for EMB, and for which there is limited clinical value for performing the procedure, there remains a need for a non-invasive monitoring techniques to monitor the tissue properties of the heart.

Cardiac magnetic resonance imaging (MRI) using late gadolinium enhancement has been recognized as the non-invasive gold standard for detecting macroscopic cardiac fibrosis. Gadolinium infiltrates the extracellular space but is not absorbed by the cells; using T1 mapping, fibrosis is distinguished from normal myocardium by an increased volume of gadolinium (de Haas et al., 2014). A reported positive correlation between gadolinium-enhanced cardiac MRI and EMB demonstrates excellent spatial and contrast resolution (Çelik et al., 2020). However, due to poor contrast, the sensitivity for detection of diffuse or early fibrosis is limited (de Haas et al., 2014). The ability to monitor progressive changes in the cardiac ECM prior to irreversible fibrosis is vital to enabling early detection and rapid intervention, thereby slowing the development of HF.

Molecular MRI involving the use of MRI-dedicated probes that enable monitoring of ECM components are currently undergoing pre-clinical evaluation (Pinkert et al., 2018). Gadolinium-based probes or manganese (MnII) or iron (FeIII)-containing nanoparticles intended to image ECM proteins, such as collagen, elastin, fibrin, and fibrinogen, are in development (Digilio et al., 2022). An MRI probe designed to image enzymes heavily implicated in the cardiac repair process, such as MMPs, has also been explored, but has achieved only limited

success (Digilio et al., 2022; Olson et al., 2010; Quillard et al., 2011; Schellenberger et al., 2008).

Nuclear imaging enables monitoring of early molecular changes without the use of invasive surgical procedures. The identification of a pathological process or monitoring therapeutic changes are difficult unless a gross morphological change is present, thus limiting anatomical imaging for advanced disease imaging (Cherry et al., 2012). Despite relatively poor spatial resolution in comparison to other biomedical imaging techniques, nuclear imaging techniques such as single-photon emission computed tomography (SPECT) and position emission tomography (PET) demonstrate superior sensitivity, enabling the detection of physiological disruption before visible disease manifestation (Angelidis et al., 2017; Cherry et al., 2012). PET is frequently considered the gold standard of molecular imaging techniques given its desirable imaging properties and optimal spatial resolution (Angelidis et al., 2017; Rowe & Pomper, 2021). PET imaging enables quantitative analysis of radioactivity concentration *in vivo* (Dewey et al., 2020). Additionally, kinetic modeling parameters may be used during PET analysis to produce a quantitative value descriptive of the tracer behavior and uptake.

The use of cardiac PET imaging has previously been limited due to lack of accessibility, cost, and technological restrains in comparison to alternative single-photon emission computed tomography (SPECT) nuclear imaging techniques (Horgan & Heller, 2021). However, superior performance and commitment to improving availability of PET and cyclotron facilities has led to a growing clinical support for the imaging modality (Davidson et al., 2018). PET exhibits improved spatial resolution and sensitivity in comparison to SPECT imaging. Furthermore, previous investigation regarding the evaluation of myocardial ischemia has indicated PET imaging provides greater diagnostic accuracy in comparison to SPECT and anatomical imaging

modality CT angiography (Danad et al., 2017). The increased diagnostic accuracy has the potential to decreases financial and resource burden on the health care system, further supporting PET imaging (Kini et al., 2019). It is noted that PET imaging requires the use of ionizing radiation, and requires careful concerning to prevent unnecessary radiation exposure, however due to the short half-life of positron-emitting isotopes, the radiation risk in comparison to traditional myocardial perfusion imaging using SPECT is modest (Desiderio et al., 2018). Given hybrid PET/CT imaging systems have become increasingly routine, and the advent of PET/MRI, diagnostic accuracy can be maximized.

However, the advancement of PET technology and the development of novel PET radiotracers has contributed to its increased feasibility. The acceptance of PET imaging has generated a demand for the development of new radiopharmaceuticals to evaluate various physiological and pathological processes. Additionally, kinetic modeling parameters may be used during PET analysis to produce a quantitative value descriptive of the tracer behavior and uptake. Currently, PET radiotracers for ECM imaging are undergoing development and pre-clinical evaluation.

1.6.1 MMP-Targeted Molecular Radioactive Imaging Probes

The development of MMP-labelled diagnostic agents has emerged as a strategy to enable non-invasive *in vivo* evaluation of MMP expression. In general, the mechanism of protease imaging is possible via 2 methods: the tracer structure may behave like the MMP, thereby binding to an active region of the enzyme; or the tracer mimics a degradable substrate which is subsequently degraded by the enzyme enabling detection by the imaging system, and becomes detectable upon degradation (Davidson et al., 2018; Quillard et al., 2011). The unique structure

of MMP-2, -7, -8, -9, -12 and -13 have proved as suitable candidates for radio-labeling and radio-fluorination for a variety of diseases and conditions, including neurological, oncology, and cardiovascular applications (van de Wiele & Oltenfreiter, 2006). Whereas MMP inhibitors have achieved limited success as therapeutic agents due to adverse side effects resulting from the high concentration of inhibitors needed to achieve an effect, they have been recognized as a potential diagnostic agent given only a low concentration is necessary to image activated MMPs (Rangasamy et al., 2019).

A variety of novel radiotracers targeting MMPs are currently in development, however, few have been used to investigate post-MI remodeling. Single photon emission computed tomography (SPECT) radiotracer [^{99m}Tc] RP805 has been used for pre-clinical cardiac imaging with relative success (Boutagy et al., 2020; Sahul et al., 2011; Su et al., 2005). Kiugel et al. (2018) demonstrated the considerable diagnostic potential of gallium-68-1,4,7,10-tetraazacyclododecane-1,4,7,10-tetraacetic acid conjugated MMP-2/9 targeting tracer ([^{86}]Ga-DOTA-TCTP-1) peptide to evaluate post-infarction remodeling, where it revealed compelling biodistribution synchronous with established patterns of MMP activation in the post-MI heart. However, the radiotracer demonstrated unfavourable stability, thus was not recommended for further evaluation and use.

Fluorine-18-(R)-2-(N-benzyl-4-(2-[^{18}F]fluoroethoxy)phenylsulphonamido)-N-hydroxy-3-methylbutanamide compound ([^{18}F]BR-351) is a pan MMP-inhibitor radiofluorinated molecular probe. [^{18}F]BR351 is a broad spectrum selective nonpeptidyl hydroxamate-based MMP inhibitor that exhibits an affinity for activated forms of MMP2, 8, 9, and 13 with recorded half-maximal inhibitory concentrations (IC_{50}) values of 4, 2, 11, and 50 nM, respectively, but does not recognize its latent forms (Wagner et al., 2011; Zinnhardt et al., 2015). Extensive evaluation has

been performed to establish the tracer's physical, chemical and biological properties, including determination of log D values, *in vitro* enzyme inhibition assays, *ex vivo* biodistribution and blocking studies, and plasma metabolism analysis (Buchler et al., 2022; Vazquez et al., 2017; Wagner et al., 2011). To date, the radiotracer has been investigated for use in the pre-clinical imaging of colorectal cancer (Vazquez et al., 2017), glioma (Zinnhardt et al., 2017), ischemic stroke (Barca et al., 2020; Zinnhardt et al., 2015), and atherosclerosis (Buchler et al., 2022) with varying efficacies. [^{18}F]BR351 has not been previously established for cardiac imaging; however, given the established role of MMPs in ventricular remodeling, the tracer has considerable promise.

2. Research Plan

2.1. Rationale

The ability of collagen-based biomaterials to reduce inflammation and limit adverse LV remodeling likely involves an MMP-mediated effect. To better understand the mechanism by which the collagen matrix attenuates the remodeling process, a method to evaluate MMP activity in the post-MI myocardium *in vivo* is desired. In this study, a fluorine-18 labelled broad-spectrum MMP tracer ([^{18}F]BR351) was investigated to establish its feasibility as an agent to detect MMP levels in the heart. *In vivo* PET imaging using [^{18}F]BR351 was compared to *ex vivo* standards, including immunohistochemistry and histology, to validate its use for cardiac imaging. The focus of evaluation was MMP2 and MMP9, given the tracer affinity and the known role of MMP2 and MMP9 in post-MI remodelling. Subsequently, the tracer was used to evaluate the therapeutic efficacy of a collagen biomaterial therapy administered to mice post-MI.

2.2. Aims and Objectives

1. To establish the pattern of [^{18}F]BR351 binding using a murine model of MI.
2. To determine if [^{18}F] distribution correlates with established patterns of MMP activation in post-MI remodeling.
3. Utilize [^{18}F]BR351 to evaluate MMP activation post-MI after treatment with a collagen hydrogel.

2.3. Hypotheses

1. Administration of [^{18}F]BR351 post-MI will exhibit increased uptake in the infarct region of the heart.
2. The collagen matrix therapy will decrease MMP activation in the post-MI heart, which will be identified by a decrease in the uptake of [^{18}F]BR351.

3. Materials and Methods

3.1. *In Vivo* Experimental Protocol

An experimental MI mouse model was utilized for completing the research objectives. Female mice C57Bl/6J (strain no. 000664) aged 8-10-weeks old were purchased from Charles River. The use of female mice was selected given increased survival following an acute MI (Pullen et al., 2020). Furthermore, whereas women exhibit a lower risk of developing CVD compared to men, women are less likely to receive immediate revascularization, therefore represent a large cohort of the target patient population that have received delayed care (Lindsey et al., 2021; Pullen et al., 2020). Following arrival at the University of Ottawa Heart Institute animal care facility, animals were allowed 1-week to acclimate prior to use. All *in vivo* experimentation was approved by the University of Ottawa Animal Care Committee (protocol number HI-3097) and in accordance with the National Institute of Health Guide for the Care and Use of Laboratory Animals.

3.1.1. Study 1: Evaluating [^{18}F]BR351 for MI Imaging

The mice underwent echocardiography imaging and PET imaging prior to the surgical procedure to establish the health baseline time point as a control. Mice were assigned to undergo surgical ligation of the left anterior descending (LAD) coronary artery to induce myocardial infarction, or sham procedure by a trained animal technician. Prior to the surgical procedure, animals received a treatment of buprenorphine delivered via intra-peritoneal injection to minimize post-surgical discomfort and distress. To induce the MI, animals were anesthetized using 2.5% isoflurane, intubated, and maintained under mechanical ventilation. A thoracotomy

to expose the heart via the fourth intercostal was performed. The LAD millimeters between the left atrium and LV was permanently ligated. Alternatively, animals underwent a sham procedure where the animal experienced a thoracotomy but did not undergo surgical ligation of the LAD. Repeat PET and echocardiography imaging was performed at i) 1-week ii) 2-weeks and iii) 4-weeks following the LAD ligation or sham operation. The time points were selected to correspond with notable MMP peak activity in a murine model according to available literature (DeLeon-Pennell et al., 2014; Lindsey & Zamilpa, 2012; Tao et al., 2004). Mice were sacrificed at 28 days post-LAD and hearts were harvested for histology (Fig. 2).

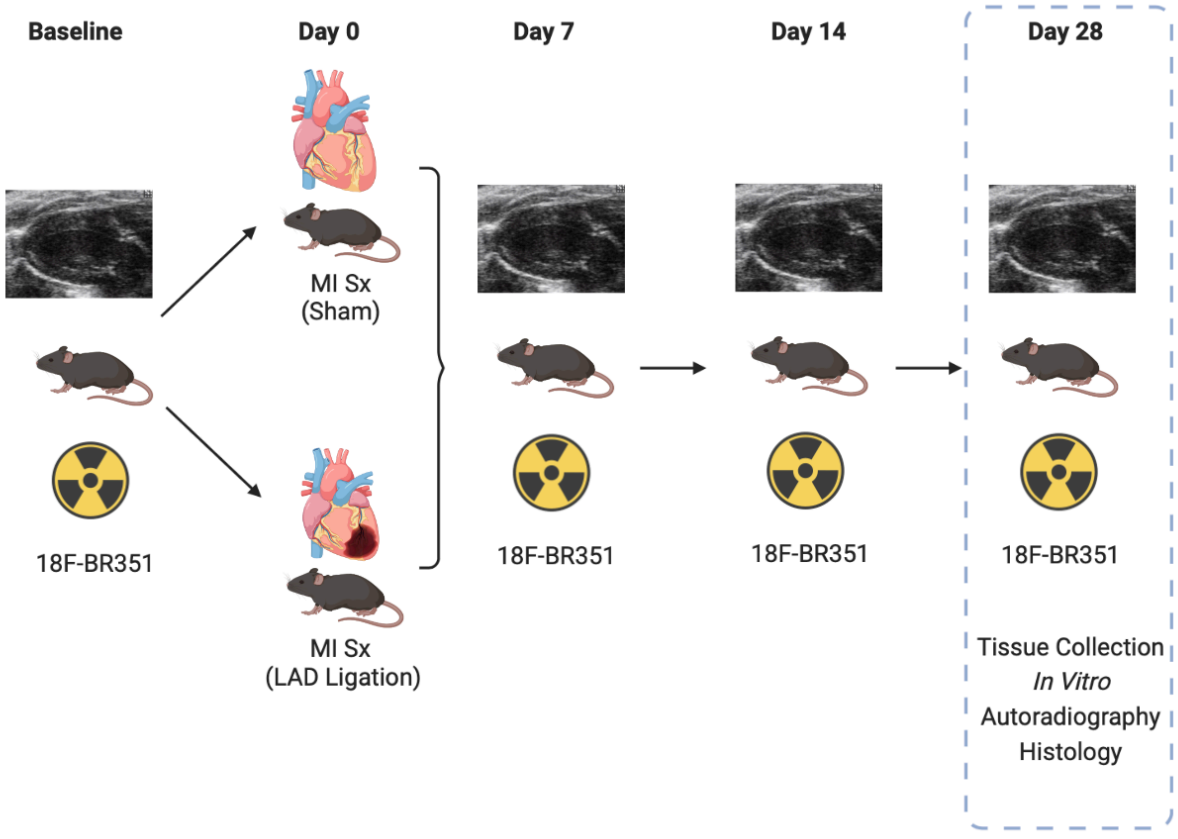

Figure 2. Experimental timeline for study 1. (A) In study 1, C57BL16 mice will undergo echocardiography and PET imaging using [^{18}F]BR351. Animals will undergo a LAD-ligation to induce a MI or sham procedure. Serial echocardiography imaging will be performed at 1, 2, and

4 weeks after ligation. Tissue collection will be performed 28 days post-MI for histological analysis. Made with BioRender©.

3.1.2. Study 2: Evaluate Post-MI MMP Activation Following Collagen Hydrogel Therapy

Animals underwent LAD ligation as previously described. Baseline echocardiography and PET imaging was performed on Day 7 post-MI. Following the completion of necessary imaging (as described above), animals were randomized to receive a control treatment (phosphate-buffered saline) or recombinant rat tail collagen type I hydrogel treatment on day 7 post-MI. The selected time-point of therapy administration is selected according to previous results as a model for MI patients who receive delayed care, where it was determined the administration of the injectable material during the proliferative phase may reduce adverse remodeling. Prior to the administration of the control or hydrogel, animals received intraperitoneal injection of buprenorphine to alleviate potential discomfort. The respective treatment was administered via 5 intramyocardial injection of the collagen hydrogel (10 uL per injection, 50 uL total, 27-gauge needle) to the border zone region under echocardiography guidance using a micromanipulator to position the syringe for delivery of the treatment. Follow-up echocardiography and PET imaging was performed at i) day 7 and, ii) day 28 post-treatment. Mice were sacrificed 4-weeks post treatment and cardiac tissue was processed for histological investigation (Fig. 3).

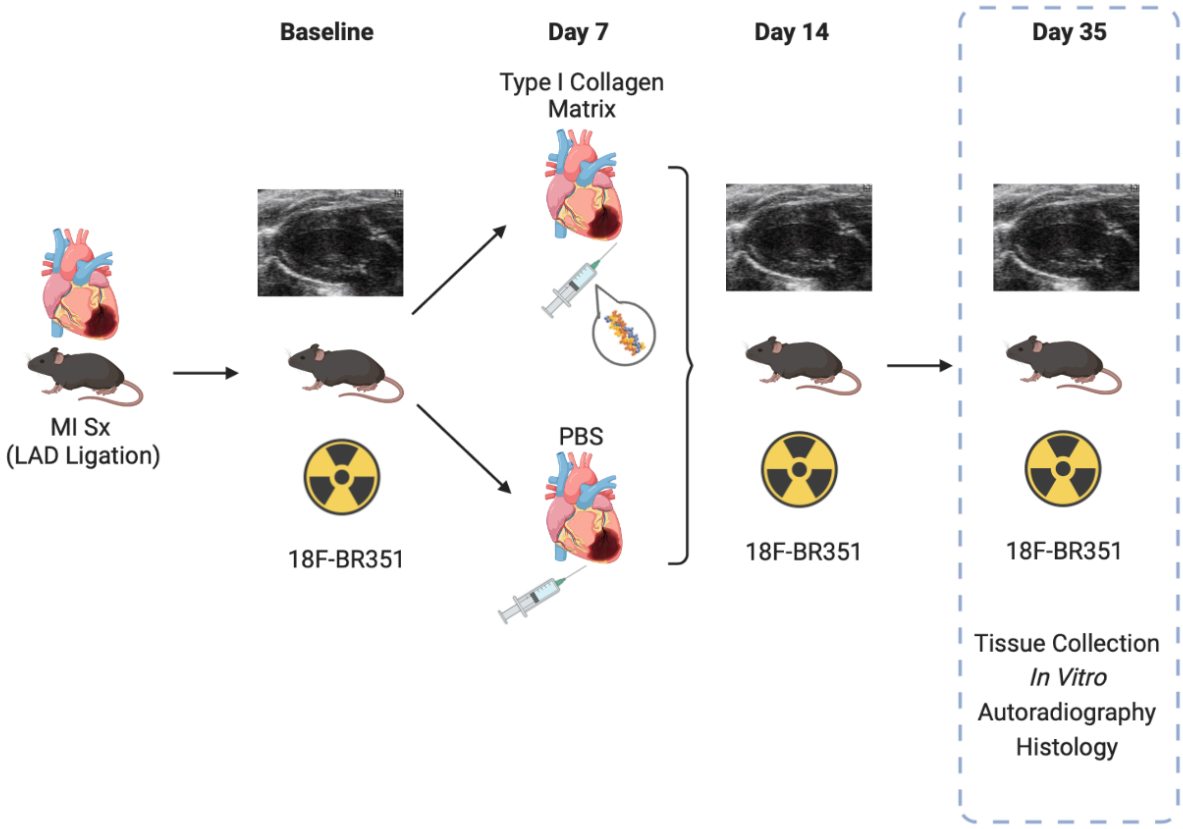

Figure 3. Experimental timeline. (B) In study 2, C57BL16 mice will undergo LAD ligation to induce MI. At day 7, animals will undergo baseline echocardiography and PET imaging using [^{18}F]BR351. Following its completion, animals will receive an echo-guided intramyocardial injection of rat tail type I collagen hydrogel or PBS. Follow-up imaging will be performed 2 weeks and 5 weeks post-MI. Made with BioRender©.

3.2. Preparation of Hydrogel

Following previous methods (Blackburn et al., 2015), 1% rat tail collagen type 1 Corning, Cat#354 236) and 40% glycosaminoglycan chondroitin sulfate C solution will be cross-linked with agents N-ethyl-N-(3-dimethylaminopropyl) carbodiimide (EDC) and N-hydroxysuccinimide (NHS). The preparation was performed in a syringe system to ensure complete mixing. The collagen matrix will be pH adjusted to achieve a pH between 6.9 – 7.2).

The collagen hydrogel was stored on ice to maintain liquid viscosity until exposure to physiological temperature upon administration.

3.3. Positron Emission Tomography Imaging

Pre-clinical PET imaging was performed using a Siemens Inveon® Dedicated microPET (D-PET) scanner (Siemens). Animals were anesthetized using 2-3 percent isoflurane in 100% oxygen. To administer [^{18}F]BR351 intravenously, a catheter was inserted into a lateral tail vein. The catheters were constructed using PE10 tubing and 30-gauge needles (BD). To prevent air embolism and the formation of thrombi, the catheters were primed using a 0.9% saline solution containing 10% heparin. Prior to intravenous catheterization, the animals' tail was sterilized using an alcohol wipe (LorisTM). Upon insertion, 10 to 50 uL of heparinized saline solution was injected to confirm catheter patency. After confirmation of successful catheterization, the catheter was secured using Vetbond tissue adhesive (3M) before transferring the animals to the imaging bed.

For all PET studies, a 10-minute transmission scan using a cobalt-57 point source was performed to correct for attenuation. Following the completion of the transmission scan, the PET emission scan commenced. Approximately 5 to 10 uCi/mg of [^{18}F]BR351 was delivered to the animal via bolus injection. After completion of the radiotracer injection, 50 uL of the heparinized saline solution was administered to promote the delivery of the radiotracer in its entirety. Dynamic PET images were acquired for 30 to 90 minutes post-injection. During *in vivo* imaging, the animals were kept warm using a heat lamp placed adjacent to the PET scanner to maintain normal physiological conditions and monitored regularly.

Following the completion of the PET imaging, the catheter was removed, and flexible caustic applicators (MedPro) were used to cauterize any blood. All catheters and syringes used in the delivery of the [^{18}F]BR351 were assayed in the dose calibrators and residual activity was documented. The animals were returned to their cage and monitored for proper recovery prior to their return to the animal facility.

The PET images were reconstructed using the Inveon Acquisition Workplace (IAW) software. An ordered subset expectation maximization (OSEM) image reconstruction algorithm available within IAW was implemented to generate the images. The images underwent correction for random, scatter, and coincidence events using IAW.

The radiotracer was produced by the Molecular Imagine Probes and Radiochemistry Laboratory at the University of Ottawa Heart Institute using the cyclotron and radiochemistry facilities.

3.4. Image Processing

Images underwent preliminary processing using Amide© software to crop the data set and to better visualize the myocardium. The images were exported as Siemen image files for analysis in FlowQuant (UOHI, Ottawa, ON). The image processing settings were modified to enable re-orientation based on the uptake frame where peak uptake was demonstrated in the myocardium – approximately 1-5 minutes following injection of [^{18}F]BR351 (frames 2-12). Initial re-orientation was performed by selecting a representative transaxial slice of the LV. To minimize the hepatic uptake visible in the frame, background liver activity was removed using the gut scale bar. A semi-ellipsoidal region of interest (ROI) was automatically placed on the generated mid-vertical long axis (VLA) and mid-horizontal long axis (HLA) images and adjusted

accordingly. Images were oriented to align the right ventricle in accordance with standard practice. The measured radioactivity was normalized to the injected activity to obtain the percent injected dose per cubic centimeter (ID/cc). To perform quantitative analysis, the defect was defined as the area of the LV with less than 75% of the normalized maximum value of the LV.

3.5. Echocardiography

Echocardiography imaging was performed using a Vevo 3100 imaging system (VisualSonics). Animals were anesthetized using 2-3% isoflurane and 100% oxygen. The hair was removed using depilatory cream (Nair) and water to create a thoracic window. The animals were transferred and secured to the imaging pad in a supine position using tape. Electrode cream was placed on extremity electrode pads to obtain the cardiac signal. Ultrasound gel was placed on the exposed chest region. Using a M440X transducer, parasternal long-axis image was obtained. Images were acquired using B-mode and electrocardiogram (ECG) kilohertz visualization (EKV). Echocardiography image analysis was performed using Vevo LAB 3.1.1. software (VisualSonics). The following parameters were calculated by manually tracing the end-systolic and end-diastolic images: LVEF, stroke volume, cardiac output, fractional shortening, end systolic volume and end diastolic volume.

3.6. Tissue Collection and Sample Preparation

At the indicated study endpoints, the animals were sacrificed via carbon dioxide asphyxiation and cervical dislocation. The hearts were removed, and the chambers were flushed with PBS to remove excess blood prior to embedding. The hearts were placed in optimized

cutting temperature (OCT) medium (Fisher) frozen using liquid nitrogen. The tissues were stored in a -20 or -80 freezer for short or long-term storage, respectively. Using a ThermoScientific HM550 Cryostat, 10-micron serial sections were obtained at different levels of the myocardium.

3.7. *In Vitro* Autoradiography

In vitro autoradiography was performed on tissue sections embedded in OCT and cut at 10 μm. The tissue sections were removed from -20 degree storage and dried for 30 minutes at room temperature. The sections were washed for 30 minutes in a buffer solution (Tris-HCL, pH:7.4) at room temperature to remove embedding media. The buffer was aspirated, and the tissue was subsequently submerged in [^{18}F]BR351 radiotracer (1 uCi/mL in Tris-HCL, pH 7.4) for 1 hour at room temperature. Following incubation, a final wash in buffer (2x5 minutes) and ice-cold distilled water for 30 seconds to remove excess tracer. The slides were removed from the bath and allowed to air dry completely. The slides were arranged and exposed to a super-resolution Storage Phosphor Screen (BAS-IP SR 2025 E) in an Electrophoresis Systems Autoradiography Cassette (FBXC 810) overnight. Following incubation, the phosphor screen was scanned using a Cyclone Plus Storage Phosphor System and analyzed using Optiquant Software. The results were analyzed by manually drawing regions of interest around the myocardium and infarct region to generate the relative light unit (RLU) data. RLU values were calculated and converted to units of activity using a calibrated decay-corrected standard. Using the area of the ROI, the activity density (counts/mm^2) was calculated.

3.8. Histology and Immunohistochemistry

To assess relative scar size, Masson's trichrome staining was performed, thereby enabling differentiation of viable muscle tissue (red) and collagen (blue). Masson's trichrome staining was performed according to manufacturer's guidelines (Sigma). To determine the scar size, the mid-line arc method was perfumed using ImageJ (Takagawa et al., 2007).

For immunohistochemical (IHC) staining, frozen sections were removed from the -20 freezer and allowed to dry at room temperature for 30 minutes. The tissue was washed in PBS (2x5min) to remove OCT before fixation using 4% paraformaldehyde (PFA) for 1 hour. Heat-mediated antigen retrieval (pH 6.0) was performed by immersing the slides in sodium citrate buffer and warmed at 60 degrees for 1 hour. After allowing the slides to return to room temperature, the tissue was washed in PBS with 0.2%Triton-X for cell permeabilization. The tissue was blocked using 10% fetal bovine serum (FBS) for 1 hour at room temperature. The primary antibodies were diluted at 1:100 in blocking solution and incubated overnight at 4 degrees for 16 hours. Primary antibodies were obtained from Abcam: mouse monoclonal anti-MMP2 (ab86607) and rabbit polyclonal anti-MMP9 (ab38898). Following incubation, the primary antibodies were removed by washing in PBS (3x5min). The secondary antibodies comprised of 1:1000 chicken anti-mouse for MMP2 (A21200), and 1:500 donkey anti-rabbit for MMP9 (A21207), and a DAPI counterstain were diluted in blocking solution and incubated with sections for 45 minutes at room temperature. After incubation, slides were washed 3x times in PBS. The cover slips were mounted using Prolong™ Gold Antifade mountant (ThermoFisher).

The sections were imaged using an Aperio VERSA Pathology slide scanner. Quantification was performed using ImageJ software. To assess the relative scar, the percent infarct region was calculated by determining the percent infarct region to myocardium ratio. The

percent fibrosis was determined by color thresholding the image. For immunofluorescence, images were separated into the respective colour channels. For quantification, 4 random microscopic images were obtained from the infarct and 4 from the border zones. The number of MMP2 and MMP9 positive stained cells were counted per sample to generate an average value.

3.9. Statistical Analysis

The data was analyzed using an unpaired t-test or one-way ANOVA with post-hoc Tukey correction. The results were presented as the mean +/- standard error (SE). A probability value of $p < 0.05$ was deemed statistically significant. Statistical analysis was performed using GraphPad Prism 7.0 (GraphPad Software, Inc.).

4. Results

4.1. Positron Emission Tomography Imaging

Initial imaging studies sought to evaluate [^{18}F]BR351 kinetic properties to ascertain the optimal imaging protocol. Representative μPET images demonstrating the *in vivo* biodistribution are shown in Figure 4. The tracer demonstrated rapid uptake by the myocardium from the blood pool with an initial peak uptake of 19.89 %ID/cc at 30-seconds post-injection (Fig. 5). Wash-out of [^{18}F]BR351 occurred soon after, with an uptake of 5.96 %ID/cc 2 minutes, 1.86 %ID/cc at 30 minutes and 1.30 %ID/cc at 90 minutes. No apparent re-distribution within the myocardium was observed after 90 minutes of imaging.

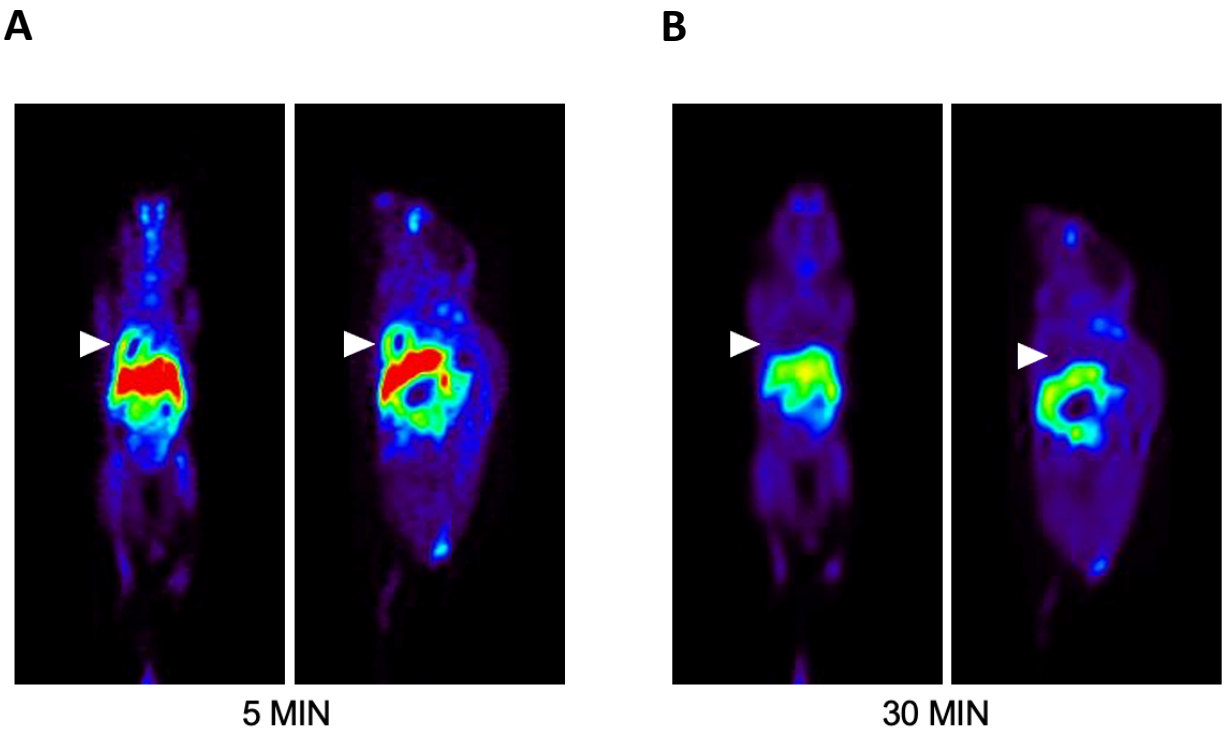

Figure 4. *In vivo* PET imaging using [^{18}F]BR351. Representative coronal and sagittal μPET images at (A) 5 minutes and (B) 30 minutes after intravenous injection of [^{18}F]BR351. The myocardium is indicated with the arrowhead.

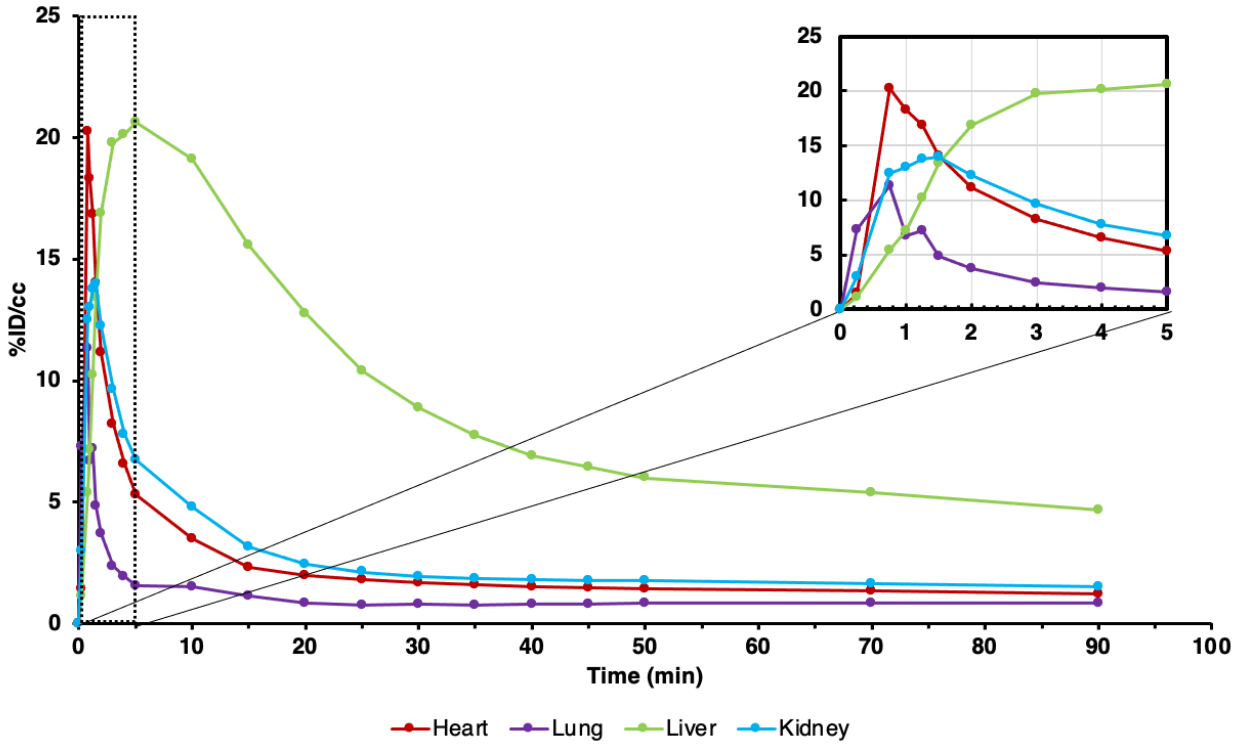

Figure 5. Time-activity curve of [^{18}F] BR351 (% ID/cc). The time activity curve for heart, lung, kidneys, and liver after injection with [^{18}F]BR351. The x-axis is zoomed in the insert to display the uptake following immediate injection of [^{18}F]BR351.

In the healthy myocardium, the distribution of [^{18}F]BR351 is relatively homogenous (Fig. 6A). Apparent non-uniformities demonstrated in polar maps is attributed to noise inherent to PET imaging due to nuclear imaging physics. The average collective size of the area with reduced uptake in the sham group was 6.4 % (Fig. 7). In the post-MI environment, a decreased uptake of [^{18}F]BR351 in the infarct region results in an apparent defect in the antero-lateral wall (Fig. 6A). The average infarct size at 7, 14, and 28 days post-MI was 32.5%, 45.5%, and 31.4% (Fig. 6B).

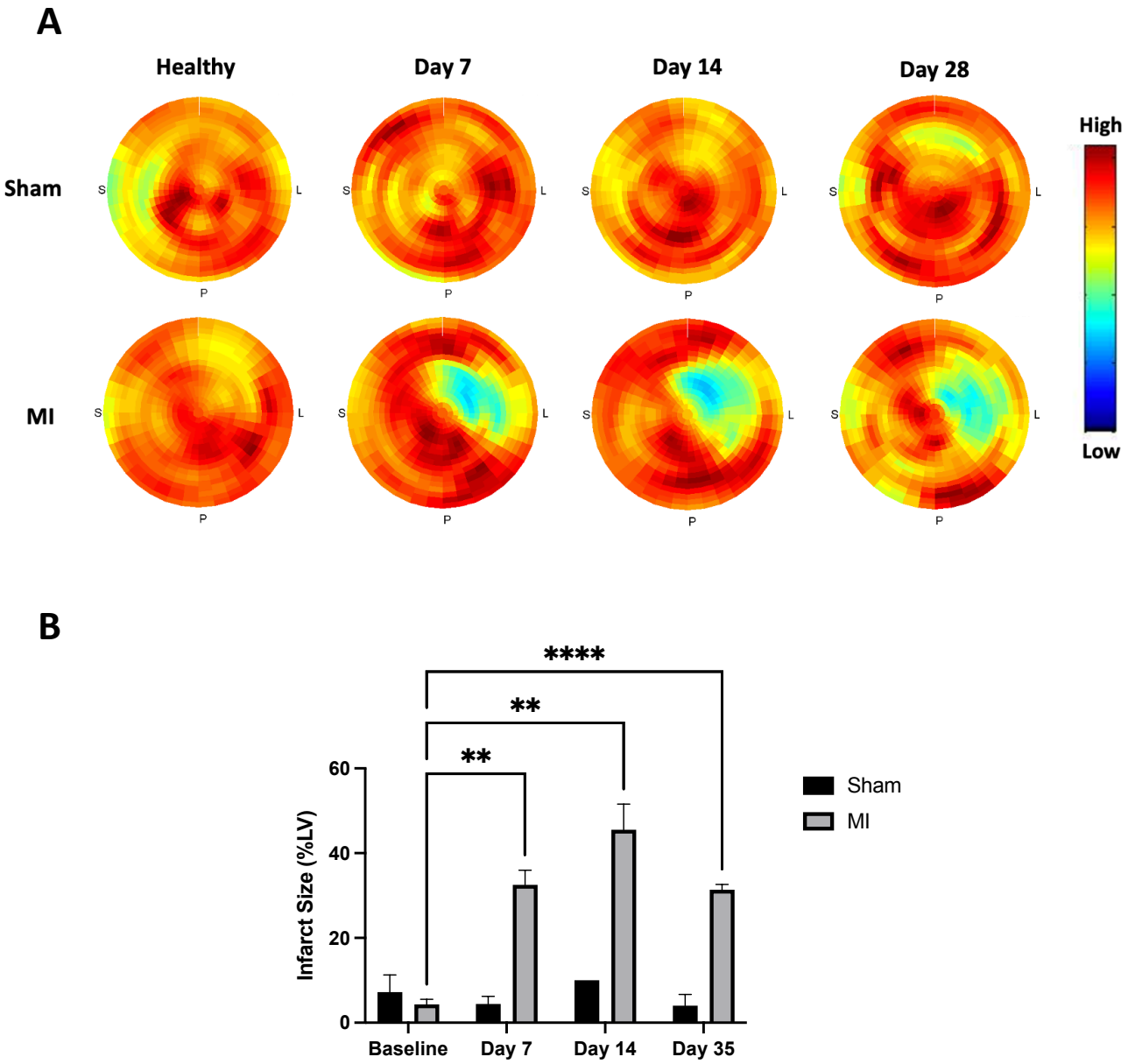

Figure 6. Representative polar maps of the net uptake of [^{18}F]BR351 in the heart. (A) [^{18}F]BR351 exhibits homogenous distribution in the healthy myocardium (n=4). After MI induction, a defect (blue/green area) is observed in the infarct region (n=5). Polar maps were generated from *in vivo* PET imaging initiated immediately upon intravenous administration of [^{18}F]BR351. (B) Defect size of sham and MI hearts. Abbreviations: s, septal; p, posterior; l, lateral. *P*-values were determined using a one-way ANOVA with a Tukey's multiple comparison test; **p < 0.01, ****p < 0.0001.

In PBS and collagen matrix treated groups, and observable difference in net tracer uptake is demonstrated in polar maps (Fig. 7A). The infarct size was calculated as the area of the LV that has less than 75% of the maximum uptake value normalized to the LV. The change in defect size was monitored to determine the therapeutic efficacy of the matrix treatment. The average defect size in animals that received PBS was 34.571%, 38.286%, and 39.286% at baseline (1-wk post-MI), week 2, and week 5, respectively (Fig. 7B). A non-significant change in the tracer uptake indicates that [^{18}F]BR351 was maintained comparable to untreated hearts. Matrix-treated hearts exhibited a significant recovery, with calculated defect sizes of 34.714%, 31.571% and 22.143% at baseline (1-wk post-MI), week 2, and week 5, respectively ($p = 0.0064$; Fig. 7B).

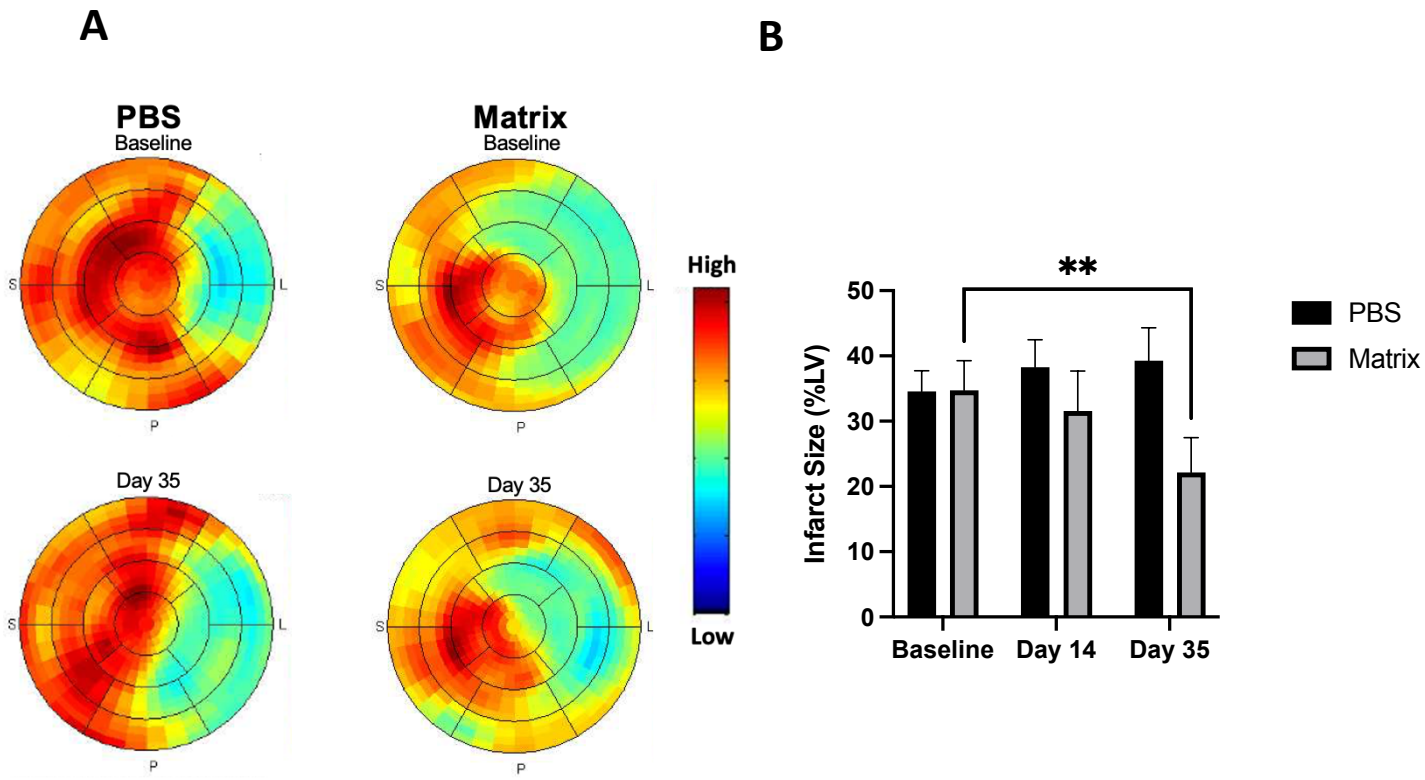

Figure 7. Change in net tracer uptake (ID/cc) in hearts treated with PBS or collagen matrix. (A) A representative polar map of hearts treated with PBS and matrix at baseline (1-wk post-MI and week 5. (B) Area of reduced tracer uptake based on net [^{18}F]BR351 distribution at baseline, 14 days, and 35 days post-MI (n = 7). *P*-values were determined using a one-way ANOVA with a Tukey's multiple comparison test; **p < 0.01.

4.2. Echocardiography

Serial echocardiography was performed on untreated hearts before ligation, and at 1, 2, and 4 weeks after the MI event. The LVEF and FS indicate a reduction in global LV systolic function after MI. The average LVEF before ligation was 59.9%, which was reduced to 33.6% after the MI (Fig. 8A). The fractional shortening decreased from 16.9% to 6.4% before and after occlusion, respectively (Fig. 8B). Cardiac output demonstrated a reduction after MI from 11.5 mL/min to 8.6 mL/min on day 7 (Fig. 8C). Subsequently, a non-significant increase in output occurred to values of 9.1 mL/min and 9.8 mL/min on 14 and 28 days, respectively. Stroke volume exhibited a similar trend with an average of 31.5 μL before ligation that was reduced to 22.2 μL after 7 days, before exhibiting a slight recovery of 23.6 μL at 14 days and 26.4 μL at 28 days (Fig. 8D). A time-dependent change in the cardiac dimensions based on end-diastolic and end-systolic volume is exhibited post-MI. The end-diastolic volume before occlusion was 54.0 μL, and exhibited a progressive increase of 60.1 μL, 73.9 μL, and 98.7 μL at 1 week, 2 weeks, and 4 weeks after MI, respectively (Fig. 8E). Similarly, pre-occlusion end-systolic volume was 21.1 μL and post-occlusion volume of 36.6 μL, 47.2 μL, 64.9 μL and 1 week, 2 weeks, and 4 weeks, respectively (Fig. 8F).

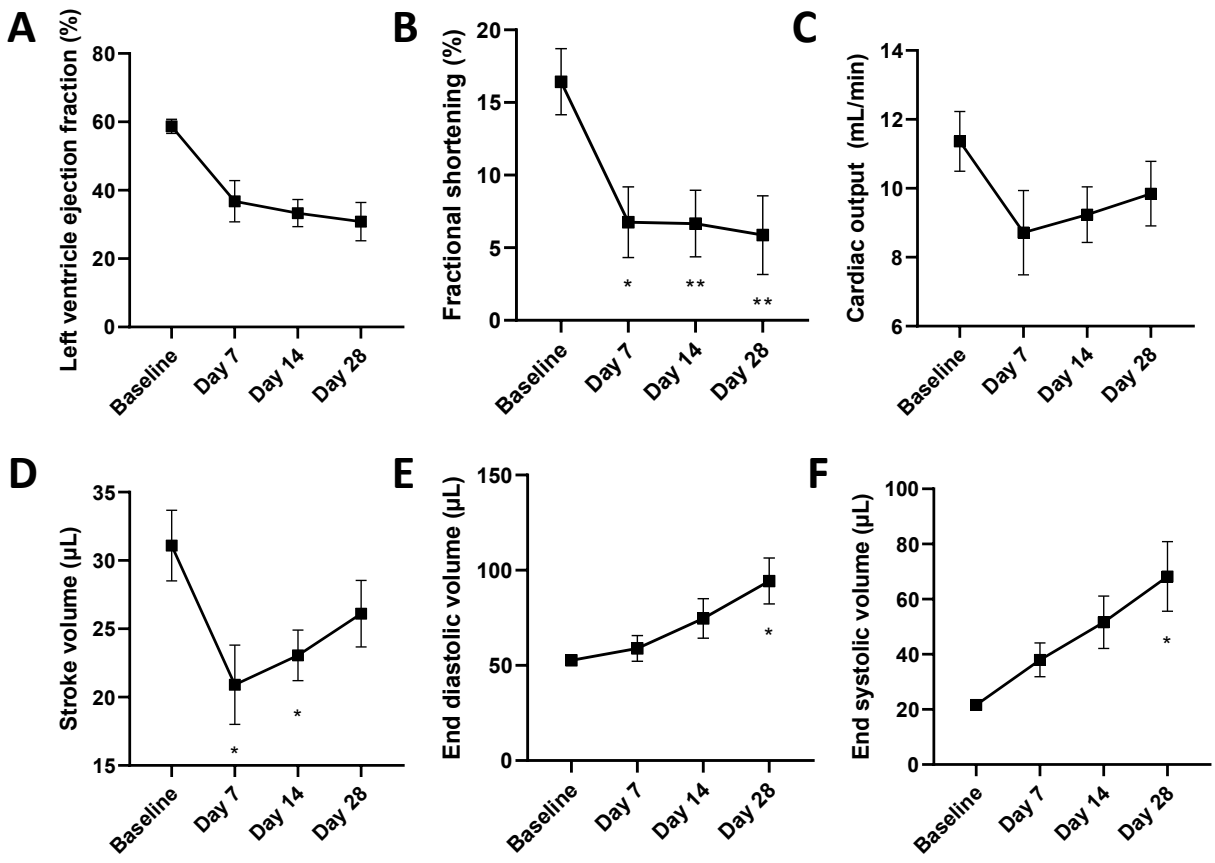

Figure 8. Cardiac function post-MI in untreated hearts. (A) Left ventricle ejection fraction (%), (B) cardiac output (mL/min), (B) fractional shortening (%), (D) stroke volume (μL), ∈ end diastolic volume (μL), (F) end systolic volume before occlusion and 1, 2, and 4-week post-LAD ligation (n= 5). *P*-values were determined using a one-way ANOVA with a Tukey's multiple comparison test; *$p < 0.05$, **$p < 0.01$.

Cardiac functional parameters were used to evaluate the therapeutic potential of the collagen hydrogel. The LVEF of PBS-treated hearts demonstrate a decrease over time relative to baseline values. In contrast, the collagen matrix group demonstrated no change in LVEF between a baseline and 28-day follow-up (Fig. 9A). When assessing the fold-change in LVEF between baseline and 28 days within each treatment group, the preservation of cardiac function for the collagen-treated hearts was significantly greater than for PBS-treated hearts (0.8 vs. 0.4,

respectively) (Fig. 9B). A similar trend of reduced stroke volume, cardiac output, fractional shortening, and end systolic and end diastolic volumes in the PBS group compared to the collagen hydrogel group was observed but did not achieve statistical significance (Fig. 9C-G).

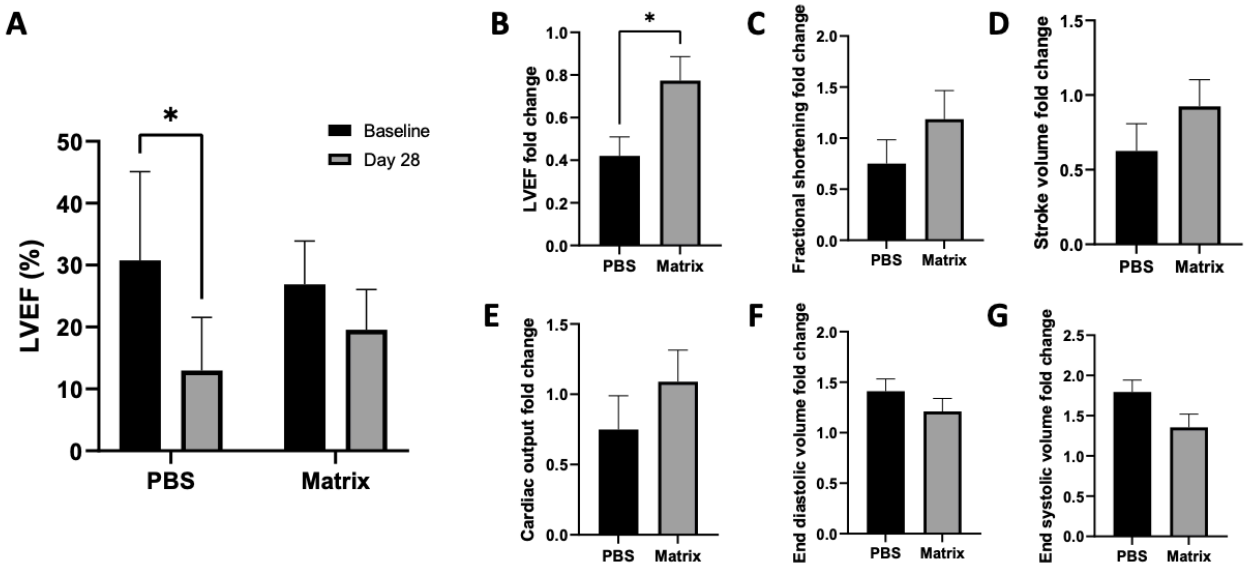

Figure 9. Change in cardiac function after collagen matrix therapy. (A) Left ventricle ejection fraction (%) at baseline and 28 days post-treatment (35 days post-ligation). Change in (A) left ventricle ejection fraction, (C) cardiac output (mL/min), (E) fractional shortening (%), (F) stroke volume (μL), (G) end diastolic volume (μL), (H) end systolic volume between baseline and 28 days post-treatment (35 days post-ligation) (n=7). *P*-values were determined via unpaired t-test; $*p < 0.05$.

4.3. Histology and Immunohistochemistry

Masson's trichrome staining was performed to measure the infarct size and extent of fibrosis in the post-MI heart (Fig. 10A). Using a standard protocol, viable myocardium (red) was non-viable fibrous collagen (blue). The analysis of histological staining demonstrated no difference in scar size between matrix and PBS-treated hearts (38.23% and 43.80% for matrix and PBS treatment groups, respectively; $p = 0.63$; Fig. 10B). However, the hearts treated with the

collagen hydrogel exhibited 9.71% fibrosis in comparison to 22.05% fibrosis in the PBS groups ($p = 0.004$; Fig. 10C).

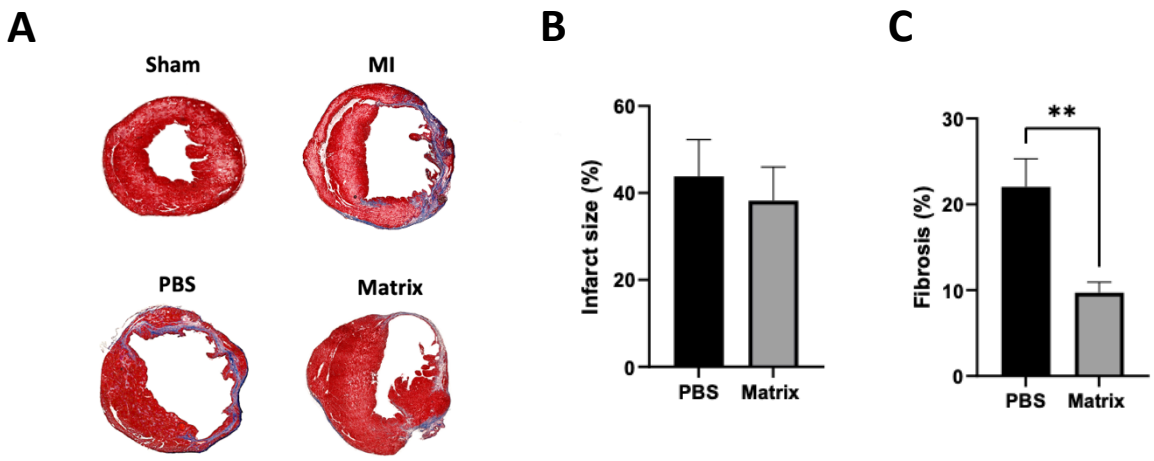

Figure 10. Masson's Trichrome staining of the heart. (A) Representative images of Masson's Trichrome staining of myocardium of a sham heart at 28 days (n=4), MI heart at 28-days post-ligation (n=5), PBS-treated MI heart at 35-days post-ligation (n=7) and collagen-treated (matrix) MI heart 35-days post-ligation (n=7). (B) Infarct size and (C) fibrosis of PBS- and collagen-treated (matrix) hearts. *P*-values were determined via unpaired t-test; $^{**}p < 0.01$.

With consideration of the binding affinity of [^{18}F]BR351 for MMPs and given the established role of MMP2 and MMP9 in ventricular remodeling, MMP2 and MMP9 expression was evaluated using immunohistochemistry. In the infarcted heart, MMP2 and MMP9 expression in the normal myocardium was negligible. However, a significant increase in MMP2 ($p = 0.014$) and MMP9 ($p = 0.036$) expression was observed in the infarct region (Fig. 11A-C).

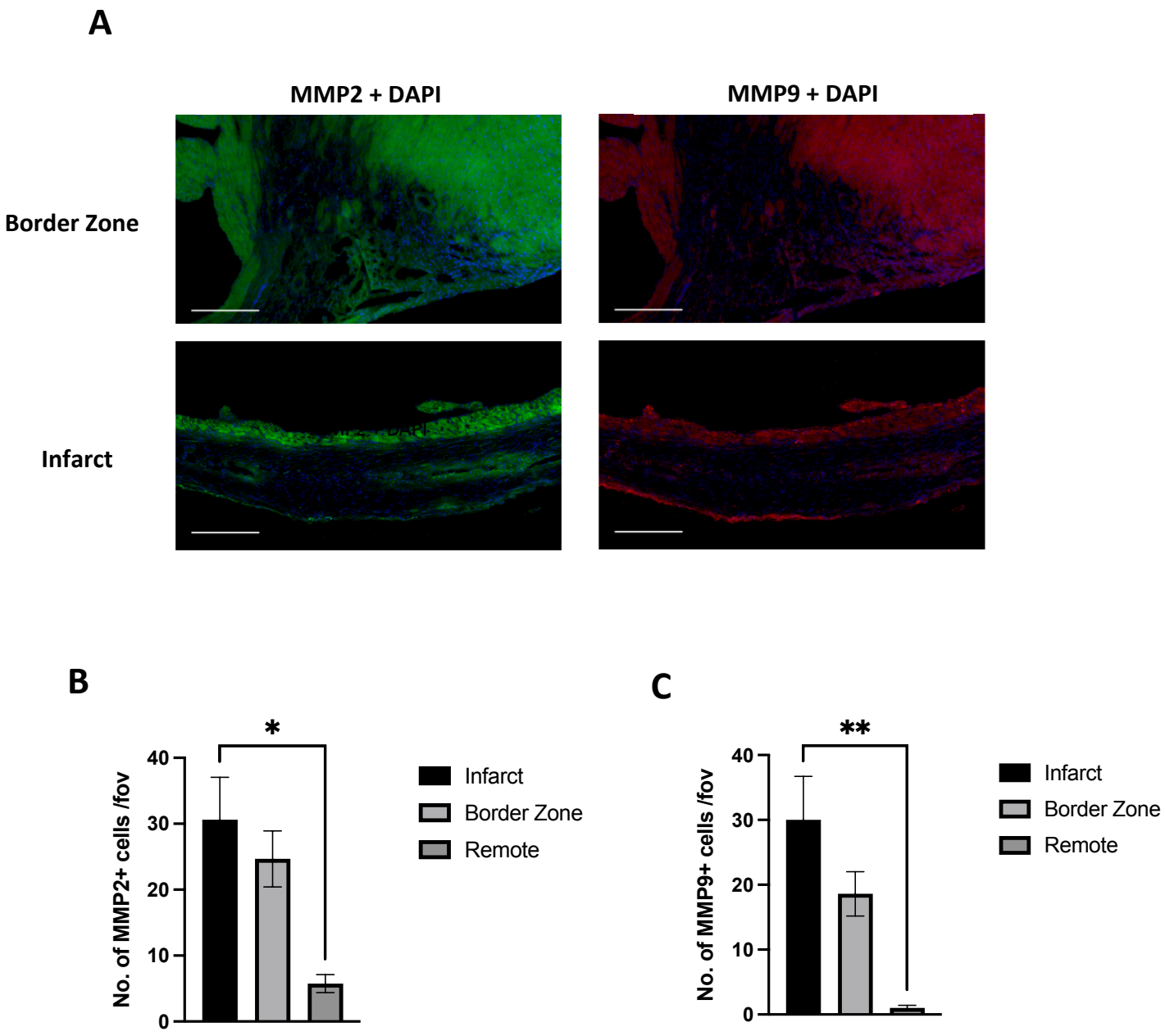

Figure 11. Immunostaining for MMP2/MMP9 of the MI heart. Sections of myocardium were stained to quantify the amount of MMP2 and MMP9 in the infarct region in untreated, PBS- and collagen-treated hearts. Microscopy images of Fluorescence of (A) MMP2 (green) and DAPI+ (blue) and MMP9 (red) and DAPI+ (blue) of infarct and border zone region. (Scale bar = 100um). (B-C) Immunohistochemistry analysis and quantification of MMP2 and MMP9 in the infarct region. *P*-values were determined using a one-way ANOVA with a Tukey's multiple comparison test; *$p < 0.05$, **$p < 0.01$.

In Study 2, there was a trend for reduced MMP2 expression in the myocardium of hearts treated with collagen matrix compared to those receiving PBS ($p = 0.0560$, n.s.; Fig. 12A-B). Likewise, immunohistochemical staining for MMP9 demonstrated a similar trend between PBS and collagen hydrogels groups ($p = 0.0697$, n.s.; Fig. 12A,C).

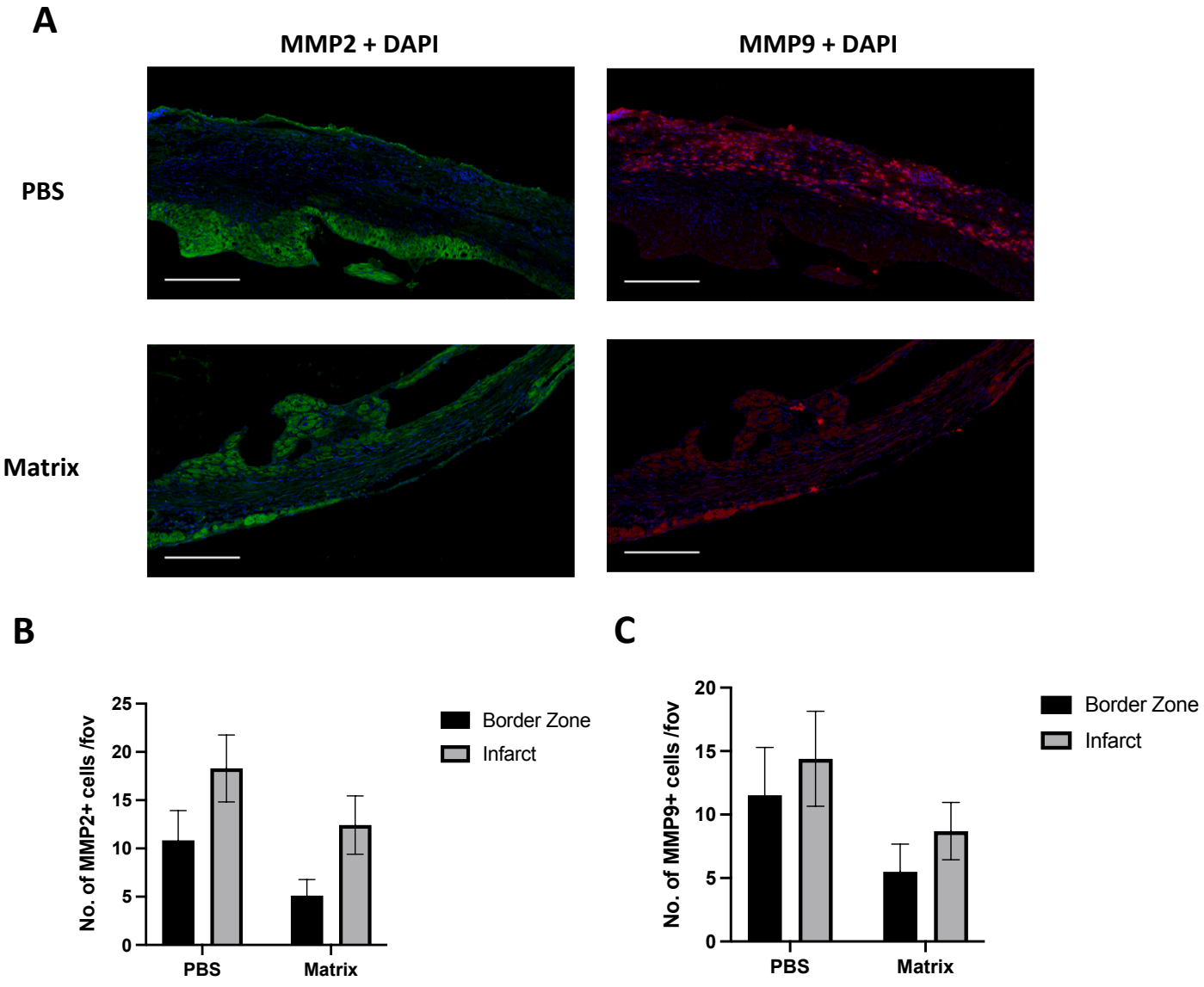

Figure 12. Immunostaining for MMP2/MMP9 in post-MI hearts treated with PBS or collagen matrix. Sections were stained to quantify the amount of MMP2 and MMP9 in the infarct region in untreated, PBS- and collagen-treated hearts. Microscopy images of Fluorescence images of hearts that received PBS or collagen treatment stained with (A) MMP2

(green), (B) MMP9 (red) and DAPI+ (blue) (Scale bar = 200um). Immunohistochemistry analysis and quantification of (B) MMP2 and (C) MMP9.

4.4. *In Vitro* Autoradiography

In vitro autoradiography of ex vivo tissue was performed to investigate specific binding of [^{18}F]BR351 to activated MMPs in the post-MI heart. Incubation of tissue sections in [^{18}F]BR351 demonstrated strong tracer binding in the healthy myocardium. In sham hearts, the tracer uptake is homogenous throughout all regions of the healthy myocardium (Fig. 13A). In the MI heart, no tracer binding was observed in the infarct region (Fig. 13A). In the border zone region, [^{18}F]BR351 is moderate, but is comparatively less than the unaffected myocardium. As a result of the tracer failing to accumulate in the infarct region, the effective tracer binding was dramatically decreased between the groups ($p = 0.037$; Fig. 13B). Overall, this coincides with the pattern of [^{18}F]BR351 biodistribution observed during *in vivo* imaging.

Autoradiography of PBS and collagen-treated hearts demonstrated a similar pattern of tracer binding (Fig. 13C). [^{18}F]BR351 binding in PBS hearts was 4.15×10^6 counts/mm^2 and 6.85×10^6 counts/mm^2 in collagen-treated hearts ($p = 0.0332$). The infarct-to-remote uptake ratio was significantly decreased in hearts treated with the collagen matrix in comparison to the PBS group ($p = 0.030$; Fig. 13D), indicating tracer uptake in the infarct region is more comparable to tracer uptake in the remote region.

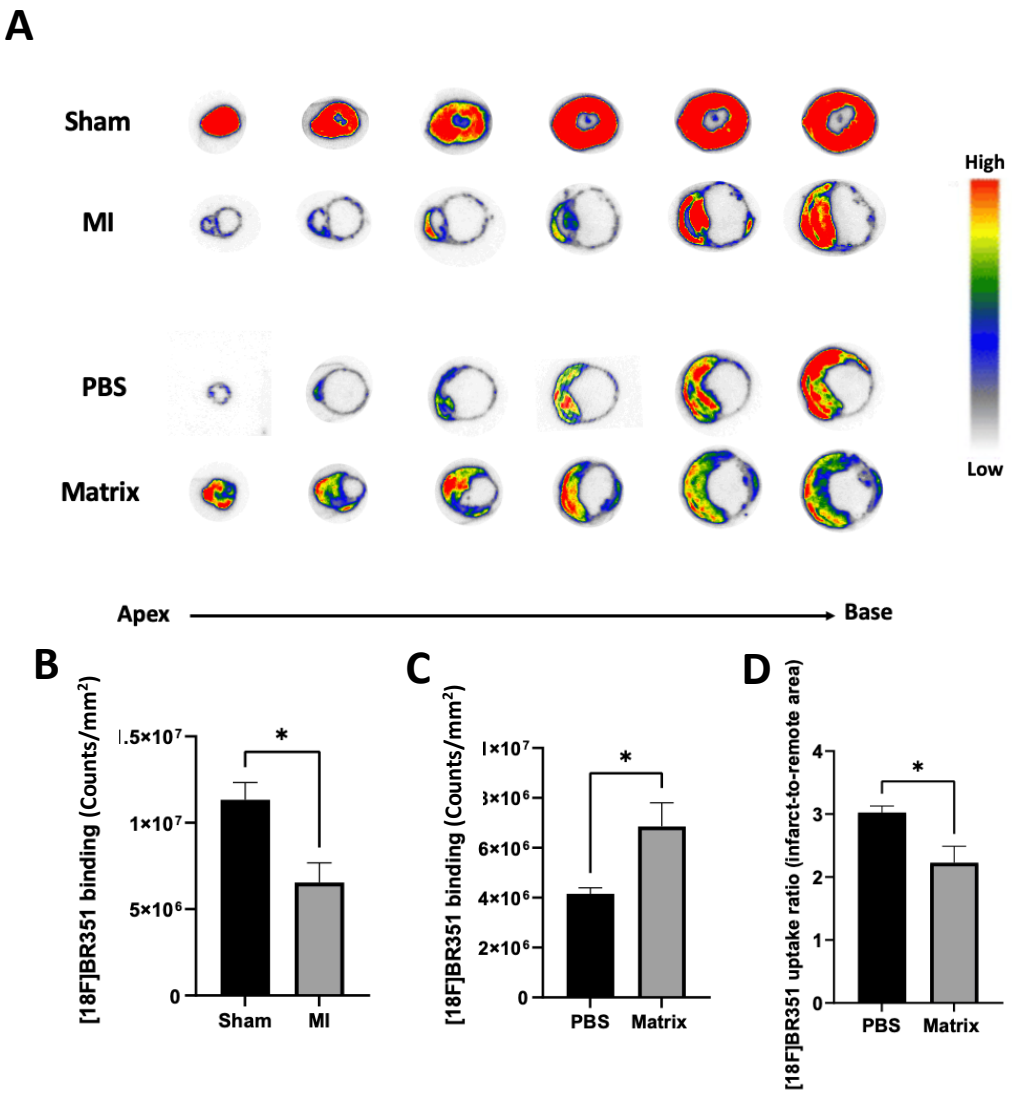

Figure 13. ***In vitro*** **autoradiography.** (A) Autoradiographs of 10-um cross-sections prepared from sham, MI, PBS-treated, and matrix-treated mice. Incubation of [^{18}F]BR351 demonstrate increased binding to the healthy myocardium. (B) Tracer binding is decreased in the infarct region, resulting in an effective decrease in tracer binding in MI hearts. (C) [^{18}F]BR351 binding is increased in hearts that received the collagen matrix. (D) The infarct-to-remote uptake ratio is reduced in the matrix treatment groups. *P*-values were determined via unpaired t-test; $*p < 0.05$.

5. Discussion

5.1. Study 1: Evaluating [^{18}F]BR351 for MI Imaging

The aim of Study 1 was to explore the use of the broad-spectrum MMP-targeted radiotracer [^{18}F]BR351 for cardiac imaging. Upon intravenous delivery of [^{18}F]BR351, the tracer accumulates in the myocardium before undergoing rapid wash-out (Fig. 4). The imaging properties coincide with a previous investigation using [^{18}F]BR351, where plasma analyte analysis demonstrated metabolism of 50 percent of the tracer within 5 minutes post-injection (Vazquez et al., 2017). The rapid distribution and washout exhibited in the myocardium is suggestive of weak or no specific binding. Where MMP activation in the healthy heart is minimized to basal levels necessary to maintain homeostasis, this phenomenon is expected. A protocol using an extended scan length of 90 minutes following injection was performed to determine if [^{18}F]BR351 may reveal an elevated concentration of radiotracer in the infarct region suggestive of delayed tracer washout, as previously demonstrated by cardiac myocardial blood flow reserve tracers, such as gallium-68- tracer 1,4,7,10-tetraazacyclododecane-N′,N″,N‴,N⁗-tetraacetic acid (Autio et al., 2020). However, delayed imaging did not reveal the redistribution [^{18}F]BR351 in the myocardium after its washout. Therefore, in conjunction with the relatively short half-life of fluorine-18, delayed imaging was not explored.

In the infarcted heart, [^{18}F]BR351 failed to accumulate in the infarct region, thus conflicting with MMP2 and MMP9 immunostaining (Fig. 11, 12). Initially, the discrepancy between the pattern of uptake exhibited during *in vivo* imaging was potentially attributable to the use of a murine model. For radiotracers which seek to delineate the infarct region post-MI, collateral circulation assists in the delivery of the radiotracer to the infarct region, despite

occlusion of one or more of the coronary arteries. However, mice lack collateral circulation in the heart, with neo-collateral circulation only forming after an ischemic event (H. Zhang & Faber, 2015). While the formation of new collaterals occurs between 1 and 2 days after coronary obstruction, it is not sufficient to prevent the formation of the necrotic core (H. Zhang & Faber, 2015). As result of impaired coronary blood flow, delivery of [^{18}F]BR351 is unable to readily penetrate the infarct zone. Given the radiotracer is unable to infiltrate to the infarct region to bind to activated MMPs, particularly during early time points in which MMP2 and MMP9 activity should be greatest, the kinetics exhibited during *in vivo* imaging may be demonstrating coronary perfusion, rather than the desired pharmacokinetics . Previous investigations by Prato et al. (2015) and Wilk (2019) regarding the imaging of myocardial inflammation post-MI suggest that a bolus injection technique may not allow sufficient opportunity for [^{18}F]FDG to accumulate inflammatory cells; similarly, rapid injection of [^{18}F]BR351 may prevent a sufficient blood concentration of the radiotracer, particularly in a murine model. However, current recommendations regarding IV infusions for animals recommends an injected volume less than 10% of the animals' body weight over a 2-hour period, and given the challenges associated with the specific activity and radioactive half-lives, its technical feasibility in a murine model is limited (Diehl et al., 2001; Turner et al., 2011).

The use of *in vitro* autoradiography enables the evaluation of tracer distribution in tissue in a manner that allows more precise localization. Furthermore, *in vitro* binding experiments eliminate the need for circulation, thus can confirm if the distribution of [^{18}F]BR351 is due to coronary blood flow. The results of *in vitro* autoradiography (Fig. 13) coincided with findings generated during *in vivo* PET imaging (Fig. 6, 7), wherein tracer uptake is increased in the healthy myocardium. Therefore, impaired coronary circulation is precluded as the cause of the

altered binding pattern of [^{18}F]BR351. However, IHC reveals an upregulation of MMP2 and MMP9 in the infarct and border zone region (Fig. 11, 12) consistent with increased cardiac ECM turnover in the affected areas consistent with findings demonstrated in current literature (Vanhoutte et al., 2006). Given *in vitro* autoradiography and *in vivo* imaging conflict with IHC results concerning MMP expression obtained from the experiments and what is reported in the literature (*i.e.*, that MMP2 and MMP9 expression increases after MI), it is suggestive that the distribution of [^{18}F]BR351 is due to non-specific binding.

The biodistribution of the tracer may be attributed to the broad-spectrum properties of [^{18}F]BR351. Consider that [^{18}F]BR351 is a broad-spectrum MMPI radiotracer that exhibits preferential binding to MMP2, 8, 9, and 13. Where MMP2 and MMP9 are the most extensively researched MMP in its role in ventricular remodeling in the post-MI heart, the temporal and spatial pattern of activation is established in literature (DeLeon-Pennell et al., 2017; Frangogiannis, 2019; Lindsey & Zamilpa, 2012; Tao et al., 2004; Vanhoutte et al., 2006). Thus, the proteases were selected as ideal candidates to confirm the ability of [^{18}F]BR351 to demonstrate ECM turnover. However, given the IC_{50} of [^{18}F]BR351 for MMP2 and MMP9 is greater than MMP8, it is possible that its sensitivity for the subtypes is insufficient for visualization during *in vivo* investigation. Similarly, consider that [^{18}F]BR351 exhibits its greatest binding to MMP8. It is possible that the selected imaging time points may not be representative of peak MMP8 activity. Thus, in conjunction with decreased sensitivity for MMP2 and MMP9 may justify the apparent *in vivo* tracer distribution. The investigation into MMP8 and MMP13 and their roles in post-MI healing may be useful to support further investigation into [^{18}F]BR351 for cardiac imaging.

Considering the function of MMP2 and MMP9 in cardiac remodeling, it is worthy to note that MMP2 has been previously identified as a housekeeping MMP, thus involved in the normal homeostasis of ECM turnover. It is possible that the accumulation of [^{18}F]BR351 in the healthy myocardium may reflect basal ECM turnover as a result of MMP2 activation. Additional performance of *in vitro* autoradiography using a specific antagonist to block the target receptor will confirm non-specific binding. If radiotracer binding remains the same following pre-incubation of a blocking agent which prevents tracer binding to target MMPs, then non-specific or off-target binding can be confirmed.

When interpretating the results of *in vivo* imaging using [^{18}F]BR351, technical limitations concerning micro-PET imaging and nuclear imaging techniques should be considered. The impaired spatial resolution native to SPECT and PET imaging techniques in comparison to other biomedical imaging modalities is further compounded due to the form factor of a murine model. Due to size limitation associated with a murine model, it is difficult to establish the kinetics of cardiac PET tracers due to spillover from the myocardium to the ventricle's blood pool (Zhong et al., 2013). Similarly, gross morphology causing apparent overlap of the liver and myocardium can result in considerable pixel spillover. Due to the hepatic metabolism of [^{18}F]BR351, interfering activity in the liver has the potential to falsely elevate apparent cardiac uptake (Saraste et al., 2020). Furthermore, the intensity of the liver uptake may create difficulty in achieving a representative scale to enable interpretation of the polar map. The ongoing refinement of nuclear imaging modalities to enable improved image resolution will assist in overcoming current challenges. Additionally, the use of combined of hybrid imaging techniques, such as PET/CT or PET/MRI, will enable more precise and accurate localization. Alternatively,

the use of a larger animal model may inherently improve the detection rate due to increased size, thereby increasing spatial resolution.

5.2. Study 2: Evaluate Post-MI MMP Activation Following Collagen Hydrogel Therapy

Molecular imaging techniques have been previously employed to evaluate the collagen hydrogel developed by the Cardiac Tissue Engineering Laboratory at the University of Ottawa. Pre-clinical PET studies have investigated effective retention of the collagen matrix (Ahmadi et al., 2015; Y. Zhang et al., 2008) and recovery of perfusion and metabolism(Ahmadi et al., 2014) following the administration of a collagen-based biomaterial containing cell additives using a murine or large animal model.

The collagen matrix demonstrated the ability to preserve cardiac function post-MI as indicated by echocardiography performance measures. The findings recapitulate the results reported by Blackburn et al., which demonstrate that delayed administration of a rat-tail type 1 collagen matrix (at 1-week post-MI) decreases the deterioration of cardiac function after MI (Blackburn et al., 2015). It is interesting to note that recent findings published by McLaughlin et al. (2019) showed the ability of recombinant human collagen matrices to reduce adverse cardiac remodelling and improve function. As discussed in that publication, this difference in performance is likely due to the superior physical properties of the recombinant human collagen materials that persist longer in the myocardium post-injection compared to the rat-tail based hydrogels. Nonetheless, although administration of the therapy was unable to recovery cardiac function, the delivery of the biomaterial demonstrated the ability to prevent further functional deterioration.

The ability to monitor ECM interactions in response to matrix therapy to ameliorate post-MI ventricular remodeling would be a valuable tool to understand the mechanisms responsible for achieving the therapeutic effect(s). The results of *in vivo* imaging and *in vitro* autoradiography indicate that the administration of the collagen matrix exhibit increased [^{18}F]BR351 binding. Given [^{18}F]BR351 was shown to accumulate in the healthy remote myocardium, increased binding demonstrated by collagen-treated hearts is suggestive of a positive therapeutic effect. Due to the discrepancy between [^{18}F]BR351uptake and immunohistochemistry, it is not possible to determine the therapeutic effect of the collagen matrix therapy to modulate MMP activation based on *in vivo* PET imaging and *in vitro* autoradiography results. It is noted that tracer binding of [^{18}F]BR351 in the PBS and matrix groups during *in vitro* autoradiography was less than or comparable to the measured binding demonstrated by the MI group which did not receive intervention. However, given an understanding of the strict temporal regulation of MMPs, it is possible the discrepancy in study length between Study 1 and Study 2 (4-weeks vs. 5 weeks) may result in the overall decreased binding of [^{18}F]BR351 observed in the treatment groups.

Due to the time-dependent nature of MMP activation, the selection of the time points to perform analysis of the proteases is critical. Additional histological investigation may be performed as a method to evaluate the effects of the collagen hydrogel therapy throughout the wound healing process to determine the ability of the collagen hydrogel to moderate MMP activation post-MI. However, histology and molecular assays require animal sacrifice, thus making it impossible to monitor MMP activity at multiple time points within the same animal. Thus, the ideal technique for monitoring MMP activity would be non-invasive and allow for serial follow-up. Serum and plasma MMP2 and MMP9 levels have demonstrated considerable

promise as a potential biomarker for predicting HF (Çelik et al., 2020; Ligi et al., 2020). However, care must be taken given when interpreting the result of MMP2 and MMP9 expression as a biomarker due to a discernible difference between MMP2 and MMP9 expression in serum and plasma levels, which must be considered when evaluating the results (Ligi et al., 2020). Additionally, serum or plasma biomarkers are an indirect measurement of MMP activity, whereas the use of PET would allow for direct non-invasive evaluation of cardiac MMP activation. As an alternative, fluorescent imaging techniques using a novel MMP-sensitive near-infrared fluorescent probe may be used as a non-invasive *in vivo* imaging technique (J. Chen et al., 2005). However, fluorescent imaging of the human heart is not yet clinically feasible due to the depth of penetration limitations of fluorescent imaging. Thus, PET imaging has remarkable potential to image the infarcted myocardium and should continue to be investigated for its potential to image MMPs.

6. Future Directions

6.1. Alternative MMP-Targeted Probes

The distribution of [^{18}F]BR351 binding conflicted with immunostaining of MMP2 and MMP9 in the MI mouse model. Alternatively, a different MMP radiotracer that is more specific in its binding may be a suitable option to evaluate ECM remodeling.

Other MMPI radiotracers have demonstrated a post-MI pattern uptake that is consistent with the hypothesized biodistribution. Most notably, the SPECT tracers [^{111}In]-DTPA-RP782 and [99mTc]RP805 have been previously used in cardiovascular imaging (Su et al., 2005). The latter demonstrated considerable promise during preliminary imaging studies due to its uptake corresponding with spatial and temporal upregulation of MMP activity in both untreated and post-reperfusion MI environments (Sahul et al., 2011; Su et al., 2005; Thorn et al., 2019) and has subsequently been used to monitor the efficacy of a novel TIMP-based post-MI treatment (Boutagy et al., 2020; Thorn et al., 2019) Other broad-spectrum MMPI radiotracers are available, and have undergone testing for other applications, but have not yet been evaluated for the purpose of cardiac imaging. For example, the radiofluorinated probe, [^{18}F]IPFP, which has an affinity for MMP9 and MMP12, may be a compelling alternative given the available information about its targets in ventricular remodeling. A previous study performed by Kondo et al. (2018) used this PET probe for cardiopulmonary imaging using a COPD model and generated compelling results due to strong agreement between in vivo PET images and histological analyses. (Kondo et al., 2018). A preliminary understanding of the behavior of [^{18}F]IPFP in the heart will expedite the process of establishing its use for cardiac imaging.

The use of a specific MMP inhibitor-bound radiotracer may assist in the elucidation of the activity of the enzyme of interest, thereby enabling a greater understanding of the underlying mechanism. For the purpose of establishing the feasibility of a tracer imaging, a tracer that exhibits binding to a single MMP will allow for easier validation and use when evaluating target to off-target binding. For instance, the use of selective radiotracer [^{18}F]FMBP, which is selective for MMP13 activation, demonstrated favourable uptake for the stratification of atherosclerosis in a murine model (Buchler et al., 2022). MMP13 is associated with the degradation of fibrillar collagen, and has been identified in ventricular remodeling, although its role is less studied in comparison to other MMP types (Wilson et al., 2003).

7. Conclusion

Although current treatments for MI result in a better quality of life and a decreased risk of mortality following the acute event, many patients are still at a risk of ventricular remodeling and developing heart failure. The development of a therapeutic collagen matrix has been previously demonstrated to reduce adverse remodeling and improve cardiac function post-MI. To better understand how the biomaterial can have a beneficial effect on cardiac remodeling, PET imaging using a broad-spectrum MMP-inhibitor [^{18}F]BR351was performed. Using a MI model, *in vivo* PET imaging and *in vitro* autoradiography revealed tracer binding in the remote region of the myocardium, but failed to accumulate in the infarct region. The administration of the collagen hydrogel revealed increased binding of [^{18}F]BR351. However, disagreement between *in vivo* PET imaging and *in vitro* autoradiography indicate that [^{18}F]BR351 is not a suitable candidate for use in a murine MI model.

8. References

Abramov, D., & Kittleson, M. M. (2021). The Universal Definition of Heart Failure: Strengths and Opportunities. *Journal of Cardiac Failure*, *27*(6), 622–624. https://doi.org/10.1016/J.CARDFAIL.2021.03.009

Ahmadi, A., McNeill, B., Vulesevic, B., Kordos, M., Mesana, L., Thorn, S., Renaud, J. M., Manthorp, E., Kuraitis, D., Toeg, H., Mesana, T. G., Davis, D. R., Beanlands, R. S., DaSilva, J. N., deKemp, R. A., Ruel, M., & Suuronen, E. J. (2014). The role of integrin α2 in cell and matrix therapy that improves perfusion, viability and function of infarcted myocardium. *Biomaterials*, *35*(17), 4749–4758. https://doi.org/10.1016/J.BIOMATERIALS.2014.02.028

Ahmadi, A., Thorn, S. L., Alarcon, E. I., Kordos, M., Padavan, D. T., Hadizad, T., Cron, G. O., Beanlands, R. S., DaSilva, J. N., Ruel, M., deKemp, R. A., & Suuronen, E. J. (2015). PET imaging of a collagen matrix reveals its effective injection and targeted retention in a mouse model of myocardial infarction. *Biomaterials*, *49*, 18–26. https://doi.org/10.1016/J.BIOMATERIALS.2015.01.016

Angelidis, G., Giamouzis, G., Karagiannis, G., Butler, J., Tsougos, I., Valotassiou, V., Giannakoulas, G., Dimakopoulos, N., Xanthopoulos, A., Skoularigis, J., Triposkiadis, F., & Georgoulias, P. (2017). SPECT and PET in ischemic heart failure. *Heart Failure Reviews*, *22*(2), 243–261. https://doi.org/10.1007/S10741-017-9594-7

Arpino, V., Brock, M., & Gill, S. E. (2015). The role of TIMPs in regulation of extracellular matrix proteolysis. *Matrix Biology : Journal of the International Society for Matrix Biology*, *44–46*, 247–254. https://doi.org/10.1016/J.MATBIO.2015.03.005

Arteaga, E., de Araújo, A. Q., Bernstein, M., Ramires, F. J. A., Ianni, B. M., Fernandes, F., & Mady, C. (2009). Valor prognóstico da fração de volume de colágeno na cardiomiopatia hipertrófica. *Arquivos Brasileiros de Cardiologia*, *92*(3), 222–226. https://doi.org/10.1590/S0066-782X2009000300010

Autio, A., Uotila, S., Kiugel, M., Kytö, V., Liljenbäck, H., Kudomi, N., Oikonen, V., Metsälä, O., Helin, S., Knuuti, J., Saraste, A., & Roivainen, A. (2020). 68Ga-DOTA chelate, a novel imaging agent for assessment of myocardial perfusion and infarction detection in a rodent model. *Journal of Nuclear Cardiology*, *27*(3), 891. https://doi.org/10.1007/S12350-019-01752-6

Badimon, L., Padró, T., & Vilahur, G. (2012). Atherosclerosis, platelets and thrombosis in acute ischaemic heart disease. *European Heart Journal. Acute Cardiovascular Care*, *1*(1), 60–74. https://doi.org/10.1177/2048872612441582

Barca, C., Foray, C., Hermann, S., Döring, C., Schäfers, M., Jacobs, A. H., & Zinnhardt, B. (2020). Characterization of the inflammatory post-ischemic tissue by full volumetric analysis of a multimodal imaging dataset. *NeuroImage*, *222*. https://doi.org/10.1016/J.NEUROIMAGE.2020.117217

Barker, T. H., & Engler, A. J. (2017). The provisional matrix: setting the stage for tissue repair outcomes. *Matrix Biology : Journal of the International Society for Matrix Biology*, *60–61*, 1. https://doi.org/10.1016/J.MATBIO.2017.04.003

Bhatt, A. S., Ambrosy, A. P., & Velazquez, E. J. (2017). Adverse Remodeling and Reverse Remodeling After Myocardial Infarction. *Current Cardiology Reports*, *19*(8). https://doi.org/10.1007/S11886-017-0876-4

Blackburn, N. J. R., Sofrenovic, T., Kuraitis, D., Ahmadi, A., McNeill, B., Deng, C., Rayner, K. J., Zhong, Z., Ruel, M., & Suuronen, E. J. (2015). Timing underpins the benefits associated with injectable collagen biomaterial therapy for the treatment of myocardial infarction. *Biomaterials*, *39*, 182–192. https://doi.org/10.1016/J.BIOMATERIALS.2014.11.004

Boateng, S., & Sanborn, T. (2013). Acute myocardial infarction. *Disease-a-Month : DM*, *59*(3), 83–96. https://doi.org/10.1016/J.DISAMONTH.2012.12.004

Bonaventura, A., Montecucco, F., & Dallegri, F. (2016). Cellular recruitment in myocardial ischaemia/reperfusion injury. *European Journal of Clinical Investigation*, *46*(6), 590–601. https://doi.org/10.1111/ECI.12633

Boutagy, N. E., Feher, A., Pfau, D., Liu, Z., Guerrera, N. M., Freeburg, L. A., Womack, S. J., Hoenes, A. C., Zeiss, C., Young, L. H., Spinale, F. G., & Sinusas, A. J. (2020). Dual Angiotensin Receptor-Neprilysin Inhibition With Sacubitril/Valsartan Attenuates Systolic Dysfunction in Experimental Doxorubicin-Induced Cardiotoxicity. *JACC. CardioOncology*, *2*(5), 774–787. https://doi.org/10.1016/J.JACCAO.2020.09.007

Bozkurt, B., Coats, A. J., Tsutsui, H., Abdelhamid, M., Adamopoulos, S., Albert, N., Anker, S. D., Atherton, J., Böhm, M., Butler, J., Drazner, M. H., Felker, G. M., Filippatos, G., Fonarow, G. C., Fiuzat, M., Gomez-Mesa, J. E., Heidenreich, P., Imamura, T., Januzzi, J., … Zieroth, S. (2021). Universal Definition and Classification of Heart Failure: A Report of the Heart Failure Society of America, Heart Failure Association of the European Society of Cardiology, Japanese Heart Failure Society and Writing Committee of the Universal Definition of Heart Failure. *Journal of Cardiac Failure*, *27*(4), 387–413. https://doi.org/10.1016/j.cardfail.2021.01.022

Brew, K., & Nagase, H. (2010). The tissue inhibitors of metalloproteinases (TIMPs): an ancient family with structural and functional diversity. *Biochimica et Biophysica Acta*, *1803*(1), 55–71. https://doi.org/10.1016/J.BBAMCR.2010.01.003

Brower, G. L., Gardner, J. D., Forman, M. F., Murray, D. B., Voloshenyuk, T., Levick, S. P., & Janicki, J. S. (2006). The relationship between myocardial extracellular matrix remodeling and ventricular function. *European Journal of Cardio-Thoracic Surgery*, *30*(4), 604–610. https://doi.org/10.1016/J.EJCTS.2006.07.006

Buchler, A., Munch, M., Farber, G., Zhao, X., Al-Haddad, R., Farber, E., & Rotstein, B. H. (2022). Selective Imaging of Matrix Metalloproteinase-13 to Detect Extracellular Matrix Remodeling in Atherosclerotic Lesions. *Molecular Imaging and Biology*, *24*(1), 93–103. https://doi.org/10.1007/S11307-021-01626-9

Burchfield, J. S., Xie, M., & Hill, J. A. (2013). Pathological Ventricular Remodeling: Mechanisms: Part 1 of 2. *Circulation*, *128*(4), 388. https://doi.org/10.1161/CIRCULATIONAHA.113.001878

Çelik, Ö., Şahin, A. A., Sarıkaya, S., & Uygur, B. (2020). Correlation between serum matrix metalloproteinase and myocardial fibrosis in heart failure patients with reduced ejection fraction: A retrospective analysis. *Anatolian Journal of Cardiology*, *24*(5), 303–308. https://doi.org/10.14744/ANATOLJCARDIOL.2020.54937

Chan, B. P., & Leong, K. W. (2008). Scaffolding in tissue engineering: general approaches and tissue-specific considerations. *European Spine Journal*, *17*(Suppl 4), 467. https://doi.org/10.1007/S00586-008-0745-3

Chen, J., Tung, C. H., Allport, J. R., Chen, S., Weissleder, R., & Huang, P. L. (2005). Near-infrared fluorescent imaging of matrix metalloproteinase activity after myocardial

infarction. *Circulation*, *111*(14), 1800–1805. https://doi.org/10.1161/01.CIR.0000160936.91849.9F

Chen, Q., Jin, M., Yang, F., Zhu, J., Xiao, Q., & Zhang, L. (2013). Matrix metalloproteinases: Inflammatory regulators of cell behaviors in vascular formation and remodeling. *Mediators of Inflammation*, *2013*. https://doi.org/10.1155/2013/928315

Cherry, S., Sorenson, J., & Phelps, M. (2012). Physics in Nuclear Medicine. In *Physics in Nuclear Medicine*. Elsevier Inc. https://doi.org/10.1016/C2009-0-51635-2

Chiong, M., Wang, Z. v., Pedrozo, Z., Cao, D. J., Troncoso, R., Ibacache, M., Criollo, A., Nemchenko, A., Hill, J. A., & Lavandero, S. (2011). Cardiomyocyte death: mechanisms and translational implications. *Cell Death & Disease 2011 2:12*, *2*(12), e244–e244. https://doi.org/10.1038/cddis.2011.130

Christia, P., Bujak, M., Gonzalez-Quesada, C., Chen, W., Dobaczewski, M., Reddy, A., & Frangogiannis, N. G. (2013). Systematic characterization of myocardial inflammation, repair, and remodeling in a mouse model of reperfused myocardial infarction. *The Journal of Histochemistry and Cytochemistry : Official Journal of the Histochemistry Society*, *61*(8), 555–570. https://doi.org/10.1369/0022155413493912

Christia, P., & Frangogiannis, N. G. (2013). Targeting inflammatory pathways in myocardial infarction. *European Journal of Clinical Investigation*, *43*(9), 986. https://doi.org/10.1111/ECI.12118

Contessotto, P., & Pandit, A. (2021). Therapies to prevent post-infarction remodelling: From repair to regeneration. *Biomaterials*, *275*, 120906. https://doi.org/10.1016/J.BIOMATERIALS.2021.120906

Cooper, L. T., Baughman, K. L., Feldman, A. M., Frustaci, A., Jessup, M., Kuhl, U., Levine, G. N., Narula, J., Starling, R. C., Towbin, J., & Virmani, R. (2007). The Role of Endomyocardial Biopsy in the Management of Cardiovascular Disease. *Circulation*, *116*(19), 2216–2233. https://doi.org/10.1161/CIRCULATIONAHA.107.186093

Costa, K. D. (2016). Decellularized Scaffold Hydrogel Materials for MI Treatment: Could "The Matrix" Really Be the Future? *Journal of the American College of Cardiology*, *67*(9), 1087–1090. https://doi.org/10.1016/J.JACC.2016.01.006

Creemers, E. E. J. M., Cleutjens, J. P. M., Smits, J. F. M., & Daemen, M. J. A. P. (2001). Matrix metalloproteinase inhibition after myocardial infarction: a new approach to prevent heart failure? *Circulation Research*, *89*(3), 201–210. https://doi.org/10.1161/HH1501.094396

Cui, N., Hu, M., & Khalil, R. A. (2017). Biochemical and Biological Attributes of Matrix Metalloproteinases. *Progress in Molecular Biology and Translational Science*, *147*, 1–73. https://doi.org/10.1016/BS.PMBTS.2017.02.005

Danad, I., Raijmakers, P. G., Driessen, R. S., Leipsic, J., Raju, R., Naoum, C., Knuuti, J., Mäki, M., Underwood, R. S., Min, J. K., Elmore, K., Stuijfzand, W. J., van Royen, N., Tulevski, I. I., Somsen, A. G., Huisman, M. C., van Lingen, A. A., Heymans, M. W., van de Ven, P. M., … Knaapen, P. (2017). Comparison of Coronary CT Angiography, SPECT, PET, and Hybrid Imaging for Diagnosis of Ischemic Heart Disease Determined by Fractional Flow Reserve. *JAMA Cardiology*, *2*(10), 1100. https://doi.org/10.1001/JAMACARDIO.2017.2471

Dauerman, H. L., & Ibanez, B. (2021). The Edge of Time in Acute Myocardial Infarction. *Journal of the American College of Cardiology*, *77*(15), 1871–1874. https://doi.org/10.1016/J.JACC.2021.03.003

Davidson, C. Q., Phenix, C. P., Tai, T. C., Khaper, N., & Lees, S. J. (2018). Searching for novel PET radiotracers: imaging cardiac perfusion, metabolism and inflammation. *American Journal of Nuclear Medicine and Molecular Imaging*, *8*(3), 200. /pmc/articles/PMC6056242/

de Haas, H. J., Arbustini, E., Fuster, V., Kramer, C. M., & Narula, J. (2014). Molecular imaging of the cardiac extracellular matrix. *Circulation Research*, *114*(5), 903–915. https://doi.org/10.1161/CIRCRESAHA.113.302680

DeLeon-Pennell, K. Y., de Castro Brás, L. E., Iyer, R. P., Bratton, D. R., Jin, Y. F., Ripplinger, C. M., & Lindsey, M. L. (2014). P. gingivalis lipopolysaccharide intensifies inflammation post-myocardial infarction through matrix metalloproteinase-9. *Journal of Molecular and Cellular Cardiology*, *0*, 218. https://doi.org/10.1016/J.YJMCC.2014.09.007

DeLeon-Pennell, K. Y., Meschiari, C. A., Jung, M., & Lindsey, M. L. (2017). Matrix Metalloproteinases in Myocardial Infarction and Heart Failure. *Progress in Molecular Biology and Translational Science*, *147*, 75–100. https://doi.org/10.1016/BS.PMBTS.2017.02.001

Deleon-Pennell, K. Y., Tian, Y., Zhang, B., Cates, C. A., Iyer, R. P., Cannon, P., Shah, P., Aiyetan, P., Halade, G. v., Ma, Y., Flynn, E., Zhang, Z., Jin, Y. F., Zhang, H., & Lindsey, M. L. (2016). CD36 Is a Matrix Metalloproteinase-9 Substrate That Stimulates Neutrophil Apoptosis and Removal During Cardiac Remodeling. *Circulation. Cardiovascular Genetics*, *9*(1), 14–25. https://doi.org/10.1161/CIRCGENETICS.115.001249

Desiderio, M. C., Lundbye, J. B., Baker, W. L., Farrell, M. B., Jerome, S. D., & Heller, G. v. (2018). Current Status of Patient Radiation Exposure of Cardiac Positron Emission Tomography and Single-Photon Emission Computed Tomographic Myocardial Perfusion Imaging. *Circulation. Cardiovascular Imaging*, *11*(12), e007565. https://doi.org/10.1161/CIRCIMAGING.118.007565

Dewey, M., Siebes, M., Kachelrieß, M., Kofoed, K. F., Maurovich-Horvat, P., Nikolaou, K., Bai, W., Kofler, A., Manka, R., Kozerke, S., Chiribiri, A., Schaeffter, T., Michallek, F., Bengel, F., Nekolla, S., Knaapen, P., Lubberink, M., Senior, R., Tang, M. X., … Schreiber, L. (2020). Clinical quantitative cardiac imaging for the assessment of myocardial ischaemia. *Nature Reviews. Cardiology*, *17*(7), 427–450. https://doi.org/10.1038/S41569-020-0341-8

di Franco, S., Amarelli, C., Montalto, A., Loforte, A., & Musumeci, F. (2018). Biomaterials and heart recovery: cardiac repair, regeneration and healing in the MCS era: a state of the "heart." *Journal of Thoracic Disease*, *10*(Suppl 20), S2346–S2362. https://doi.org/10.21037/JTD.2018.01.85

Diegelmann, R. F. (2004). Collagen Metabolism. *Wounds*, *13*(5), 520–529. https://doi.org/10.1016/B0-12-475570-4/00307-3

Diehl, K. H., Hull, R., Morton, D., Pfister, R., Rabemampianina, Y., Smith, D., Vidal, J. M., & van de Vorstenbosch, C. (2001). A good practice guide to the administration of substances and removal of blood, including routes and volumes. *Journal of Applied Toxicology : JAT*, *21*(1), 15–23. https://doi.org/10.1002/JAT.727

Digilio, G., Lacerda, S., Begoña,], Plaza, L., & Phinikaridou, A. (2022). Extracellular Matrix Targeted MRI Probes. *Analysis & Sensing*, e202200039. https://doi.org/10.1002/ANSE.202200039

el Hajj, E. C., el Hajj, M. C., Ninh, V. K., & Gardner, J. D. (2018). Inhibitor of lysyl oxidase improves cardiac function and the collagen/MMP profile in response to volume overload. *American Journal of Physiology. Heart and Circulatory Physiology*, *315*(3), H463–H473. https://doi.org/10.1152/AJPHEART.00086.2018

El-Sherbiny, I. M., & Yacoub, M. H. (2013). Hydrogel scaffolds for tissue engineering: Progress and challenges. *Global Cardiology Science & Practice*, *2013*(3), 38. https://doi.org/10.5339/GCSP.2013.38

Ertl, G., & Frantz, S. (2005). Healing after myocardial infarction. *Cardiovascular Research*, *66*(1), 22–32. https://doi.org/10.1016/J.CARDIORES.2005.01.011

Farache Trajano, L., & Smart, N. (2021). Immunomodulation for optimal cardiac regeneration: insights from comparative analyses. *NPJ Regenerative Medicine*, *6*(1). https://doi.org/10.1038/S41536-021-00118-2

Frangogiannis, N. G. (2012). Matricellular proteins in cardiac adaptation and disease. *Physiological Reviews*, *92*(2), 635–688. https://doi.org/10.1152/PHYSREV.00008.2011

Frangogiannis, N. G. (2019). The Extracellular Matrix in Ischemic and Nonischemic Heart Failure. *Circulation Research*, *125*(1), 117–146. https://doi.org/10.1161/CIRCRESAHA.119.311148

Frangogiannis, N. G., & Kovacic, J. C. (2020). JACC Focus Seminar: Extracellular Matrix in Cardiovascular Health and Disease Extracellular Matrix in Ischemic Heart Disease, Part 4/4: JACC Focus Seminar. *Journal of the American College of Cardiology*, *75*(17), 2219. https://doi.org/10.1016/J.JACC.2020.03.020

Fratzl, P., & Weinkamer, R. (2007). Nature's hierarchical materials. *Progress in Materials Science*, *52*(8), 1263–1334. https://doi.org/10.1016/J.PMATSCI.2007.06.001

French, B. A., & Kramer, C. M. (2007). Mechanisms of Post-Infarct Left Ventricular Remodeling. *Drug Discovery Today. Disease Mechanisms*, *4*(3), 185–196. https://doi.org/10.1016/J.DDMEC.2007.12.006

From, A. M., Maleszewski, J. J., & Rihal, C. S. (2011). Current Status of Endomyocardial Biopsy. *Mayo Clinic Proceedings*, *86*(11), 1095. https://doi.org/10.4065/MCP.2011.0296

Gargiulo, S., Greco, A., Gramanzini, M., Petretta, M. P., Ferro, A., Larobina, M., Panico, M., Brunetti, A., & Cuocolo, A. (2012). PET/CT imaging in mouse models of myocardial ischemia. *Journal of Biomedicine & Biotechnology*, *2012*. https://doi.org/10.1155/2012/541872

Gibb, A. A., Lazaropoulos, M. P., & Elrod, J. W. (2020). Myofibroblasts and Fibrosis: Mitochondrial and Metabolic Control of Cellular Differentiation. *Circulation Research*, *127*(3), 427–447. https://doi.org/10.1161/CIRCRESAHA.120.316958

Hadler-Olsen, E., Fadnes, B., Sylte, I., Uhlin-Hansen, L., & Winberg, J. O. (2011). Regulation of matrix metalloproteinase activity in health and disease. *The FEBS Journal*, *278*(1), 28–45. https://doi.org/10.1111/J.1742-4658.2010.07920.X

Hahn, V. S., Yanek, L. R., Vaishnav, J., Ying, W., Vaidya, D., Lee, Y. Z. J., Riley, S. J., Subramanya, V., Brown, E. E., Hopkins, C. D., Ononogbu, S., Perzel Mandell, K., Halushka, M. K., Steenbergen, C., Rosenberg, A. Z., Tedford, R. J., Judge, D. P., Shah, S. J., Russell, S. D., … Sharma, K. (2020). Endomyocardial Biopsy Characterization of Heart Failure With Preserved Ejection Fraction and Prevalence of Cardiac Amyloidosis. *JACC: Heart Failure*, *8*(9), 712–724. https://doi.org/10.1016/J.JCHF.2020.04.007

Horgan, S. J., & Heller, G. v. (2021). Widening the availability of ammonia to increase the footprint of cardiac PET. *Journal of Nuclear Cardiology : Official Publication of the*

American Society of Nuclear Cardiology, *28*(1), 300–302. https://doi.org/10.1007/S12350-019-01986-4

Horn, M. A., & Trafford, A. W. (2016). Aging and the cardiac collagen matrix: Novel mediators of fibrotic remodelling. *Journal of Molecular and Cellular Cardiology*, *93*, 175. https://doi.org/10.1016/J.YJMCC.2015.11.005

Hsieh, P. C. H., Segers, V. F. M., Davis, M. E., MacGillivray, C., Gannon, J., Molkentin, J. D., Robbins, J., & Lee, R. T. (2007). Evidence from a genetic fate-mapping study that stem cells refresh adult mammalian cardiomyocytes after injury. *Nature Medicine*, *13*(8), 970–974. https://doi.org/10.1038/NM1618

Hugenberg, V., Behrends, M., Wagner, S., Hermann, S., Schäfers, M., Kolb, H. C., Szardenings, K., Walsh, J. C., Gomez, L. F., Kopka, K., & Haufe, G. (2018). Synthesis, radiosynthesis, in vitro and first in vivo evaluation of a new matrix metalloproteinase inhibitor based on γ-fluorinated α-sulfonylaminohydroxamic acid. *EJNMMI Radiopharmacy and Chemistry 2018 3:1*, *3*(1), 1–20. https://doi.org/10.1186/S41181-018-0045-0

Hugenholtz, P. G., Fioretti, P., Simoons, M. L., Serruys, P. W., & Roelandt, J. R. T. C. (1986). Assessment for prognosis during and after myocardial infarction. A plea for a stratified approach. *Advances in Cardiology*, *34*, 58–76. https://doi.org/10.1159/000413039

Iyer, R. P., de Castro Brás, L. E., Jin, Y. F., & Lindsey, M. L. (2014). Translating Koch's Postulates to Identify Matrix Metalloproteinase Roles in Post-Myocardial Infarction Remodeling: The Cardiac Metalloproteinase Actions (CarMA) Postulates. *Circulation Research*, *114*(5), 860. https://doi.org/10.1161/CIRCRESAHA.114.301673

Jenča, D., Melenovský, V., Stehlik, J., Staněk, V., Kettner, J., Kautzner, J., Adámková, V., & Wohlfahrt, P. (2021). Heart failure after myocardial infarction: incidence and predictors. *ESC Heart Failure*, *8*(1), 222. https://doi.org/10.1002/EHF2.13144

Jugdutt, B. I. (n.d.). *Chapter 2 Extracellular Matrix and Cardiac Remodeling*.

Karamitsos, T. D., Arvanitaki, A., Karvounis, H., Neubauer, S., & Ferreira, V. M. (2020). Myocardial Tissue Characterization and Fibrosis by Imaging. *JACC. Cardiovascular Imaging*, *13*(5), 1221–1234. https://doi.org/10.1016/J.JCMG.2019.06.030

Khan, R., & Khan, M. H. (2013). Use of collagen as a biomaterial: An update. *Journal of Indian Society of Periodontology*, *17*(4), 539–542. https://doi.org/10.4103/0972-124X.118333

Kini, V., Viragh, T., Magid, D., Masoudi, F. A., Moghtaderi, A., & Black, B. (2019). Trends in High- and Low-Value Cardiovascular Diagnostic Testing in Fee-for-Service Medicare, 2000-2016. *JAMA Network Open*, *2*(10), 1913070. https://doi.org/10.1001/JAMANETWORKOPEN.2019.13070

Kiugel, M., Kytö, V., Saanijoki, T., Liljenbäck, H., Metsälä, O., Ståhle, M., Tuomela, J., Li, X. G., Saukko, P., Knuuti, J., Roivainen, A., & Saraste, A. (2018). Evaluation of 68Ga-labeled peptide tracer for detection of gelatinase expression after myocardial infarction in rat. *Journal of Nuclear Cardiology : Official Publication of the American Society of Nuclear Cardiology*, *25*(4), 1114–1123. https://doi.org/10.1007/S12350-016-0744-4

Klingberg, F., Hinz, B., & White, E. S. (2013). The myofibroblast matrix: implications for tissue repair and fibrosis. *The Journal of Pathology*, *229*(2), 298. https://doi.org/10.1002/PATH.4104

Kondo, N., Temma, T., Aita, K., Shimochi, S., Koshino, K., Senda, M., & Iida, H. (2018). Development of matrix metalloproteinase-targeted probes for lung inflammation detection with positron emission tomography. *Scientific Reports 2018 8:1*, *8*(1), 1–10. https://doi.org/10.1038/s41598-018-19890-1

Kuivaniemi, H., & Tromp, G. (2019). Type III collagen (COL3A1): Gene and protein structure, tissue distribution, and associated diseases. *Gene*, *707*, 151. https://doi.org/10.1016/J.GENE.2019.05.003

Lambert, J. M., Lopez, E. F., & Lindsey, M. L. (2008). Macrophage roles following myocardial infarction. *International Journal of Cardiology*, *130*(2), 147–158. https://doi.org/10.1016/J.IJCARD.2008.04.059

Laronha, H., & Caldeira, J. (2020). Structure and Function of Human Matrix Metalloproteinases. *Cells*, *9*(5). https://doi.org/10.3390/CELLS9051076

Lebel, R., & Lepage, M. (2014). A comprehensive review on controls in molecular imaging: lessons from MMP-2 imaging. *Contrast Media & Molecular Imaging*, *9*(3), 187–210. https://doi.org/10.1002/CMMI.1555

Li, L., Zhao, Q., & Kong, W. (2018). Extracellular matrix remodeling and cardiac fibrosis. *Matrix Biology : Journal of the International Society for Matrix Biology*, *68–69*, 490–506. https://doi.org/10.1016/J.MATBIO.2018.01.013

Ligi, D., Maniscalco, R., & Mannello, F. (2020). MMP-2 and MMP-9 in Human Peripheral Blood: Optimizing Gelatinase Calibrator for Degradome Research and Discovering a Novel Gelatinolytic Enzyme. *Journal of Proteome Research*, *19*(1), 525–536. https://doi.org/10.1021/ACS.JPROTEOME.9B00261/SUPPL_FILE/PR9B00261_SI_001.PDF

Lindsey, M. L. (2018). Assigning matrix metalloproteinase roles in ischaemic cardiac remodelling. *Nature Reviews Cardiology 2018 15:8*, *15*(8), 471–479. https://doi.org/10.1038/s41569-018-0022-z

Lindsey, M. L., Brunt, K. R., Kirk, J. A., Kleinbongard, P., Calvert, J. W., de Castro Brás, L. E., DeLeon-Pennell, K. Y., del Re, D. P., Frangogiannis, N. G., Frantz, S., Gumina, R. J., Halade, G. v., Jones, S. P., Ritchie, R. H., Spinale, F. G., Thorp, E. B., Ripplinger, C. M., & Kassiri, Z. (2021). Guidelines for in vivo mouse models of myocardial infarction. *American Journal of Physiology - Heart and Circulatory Physiology*, *321*(6), H1056–H1073. https://doi.org/10.1152/AJPHEART.00459.2021/ASSET/IMAGES/LARGE/AJPHEART.00459.2021_F001.JPEG

Lindsey, M. L., Iyer, R. P., Jung, M., DeLeon-Pennell, K. Y., & Ma, Y. (2016). Matrix metalloproteinases as input and output signals for post-myocardial infarction remodeling. *Journal of Molecular and Cellular Cardiology*, *91*, 134–140. https://doi.org/10.1016/j.yjmcc.2015.12.018

Lindsey, M. L., & Zamilpa, R. (2012). Temporal and Spatial Expression of Matrix Metalloproteinases and Tissue Inhibitors of Metalloproteinases Following Myocardial Infarction. *Cardiovascular Therapeutics*, *30*(1), 31. https://doi.org/10.1111/J.1755-5922.2010.00207.X

Linton, M. F., Yancey, P. G., Davies, S. S., Jerome, W. G., Linton, E. F., Song, W. L., Doran, A. C., & Vickers, K. C. (2000). The Role of Lipids and Lipoproteins in Atherosclerosis. *Science*, *111*(2877), 166–186. https://pubmed-ncbi-nlm-nih-gov.proxy.bib.uottawa.ca/26844337/

Little, K., Llorián-Salvador, M., Tang, M., Du, X., Marry, S., Chen, M., & Xu, H. (2020). Macrophage to myofibroblast transition contributes to subretinal fibrosis secondary to neovascular age-related macular degeneration. *Journal of Neuroinflammation*, *17*(1). https://doi.org/10.1186/S12974-020-02033-7

Liu, P., Sun, M., & Sader, S. (2006). Matrix metalloproteinases in cardiovascular disease. *The Canadian Journal of Cardiology*, *22 Suppl B*(Suppl B), 25B-30B. https://doi.org/10.1016/S0828-282X(06)70983-7

Ma, Z., Mao, C., Jia, Y., Fu, Y., & Kong, W. (2020). Extracellular matrix dynamics in vascular remodeling. *American Journal of Physiology. Cell Physiology*, *319*(3), C481–C499. https://doi.org/10.1152/AJPCELL.00147.2020

Mathew-Steiner, S. S., Roy, S., & Sen, C. K. (2021). Collagen in Wound Healing. *Bioengineering*, *8*(5). https://doi.org/10.3390/BIOENGINEERING8050063

Matrisian, L. M. (1990). Metalloproteinases and their inhibitors in matrix remodeling. *Trends in Genetics : TIG*, *6*(4), 121–125. https://doi.org/10.1016/0168-9525(90)90126-Q

Matsui, Y., Morimoto, J., & Uede, T. (2010). Role of matricellular proteins in cardiac tissue remodeling after myocardial infarction. *World Journal of Biological Chemistry*, *1*(5), 69–80. https://doi.org/10.4331/wjbc.v1.i5.69

McLaughlin, S., McNeill, B., Podrebarac, J., Hosoyama, K., Sedlakova, V., Cron, G., Smyth, D., Seymour, R., Goel, K., Liang, W., Rayner, K. J., Ruel, M., Suuronen, E. J., & Alarcon, E. I. (2019). Injectable human recombinant collagen matrices limit adverse remodeling and improve cardiac function after myocardial infarction. *Nature Communications*, *10*(1). https://doi.org/10.1038/S41467-019-12748-8

Mechanic, O. J., Gavin, M., & Grossman, S. A. (2022). Acute Myocardial Infarction. *StatPearls*. https://www.ncbi.nlm.nih.gov/books/NBK459269/

Mezzaroma, E., Toldo, S., Farkas, D., Seropian, I. M., van Tassell, B. W., Salloum, F. N., Kannan, H. R., Menna, A. C., Voelkel, N. F., & Abbate, A. (2011). The inflammasome promotes adverse cardiac remodeling following acute myocardial infarction in the mouse. *Proceedings of the National Academy of Sciences of the United States of America*, *108*(49), 19725–19730. https://doi.org/10.1073/PNAS.1108586108

Mouton, A. J., Rivera, O. J., & Lindsey, M. L. (2018). Myocardial infarction remodeling that progresses to heart failure: a signaling misunderstanding. *American Journal of Physiology. Heart and Circulatory Physiology*, *315*(1), H71–H79. https://doi.org/10.1152/AJPHEART.00131.2018

Murtha, L. A., Schuliga, M. J., Mabotuwana, N. S., Hardy, S. A., Waters, D. W., Burgess, J. K., Knight, D. A., & Boyle, A. J. (2017). The Processes and Mechanisms of Cardiac and Pulmonary Fibrosis. *Frontiers in Physiology*, *8*(OCT). https://doi.org/10.3389/FPHYS.2017.00777

Nagase, H., Visse, R., & Murphy, G. (2006). Structure and function of matrix metalloproteinases and TIMPs. *Cardiovascular Research*, *69*(3), 562–573. https://doi.org/10.1016/J.CARDIORES.2005.12.002

Nian, M., Lee, P., Khaper, N., & Liu, P. (2004). Inflammatory cytokines and postmyocardial infarction remodeling. *Circulation Research*, *94*(12), 1543–1553. https://doi.org/10.1161/01.RES.0000130526.20854.FA

Ojha, N., Dhamoon, A. S., & Chapagain, R. (2021). Myocardial Infarction (Nursing). *StatPearls*. http://www.ncbi.nlm.nih.gov/pubmed/33760446

Olson, E. S., Jiang, T., Aguilera, T. A., Nguyen, Q. T., Ellies, L. G., Scadeng, M., & Tsien, R. Y. (2010). Activatable cell penetrating peptides linked to nanoparticles as dual probes for in vivo fluorescence and MR imaging of proteases. *Proceedings of the National Academy of Sciences of the United States of America*, *107*(9), 4311–4316. https://doi.org/10.1073/PNAS.0910283107

Phatharajaree, W., Phrommintikul, A., & Chattipakorn, N. (2007). Matrix metalloproteinases and myocardial infarction. *The Canadian Journal of Cardiology*, *23*(9), 727–733. https://doi.org/10.1016/S0828-282X(07)70818-8

Pinkert, M. A., Hortensius, R. A., Ogle, B. M., & Eliceiri, K. W. (2018). Imaging the Cardiac Extracellular Matrix. *Advances in Experimental Medicine and Biology*, *1098*, 21. https://doi.org/10.1007/978-3-319-97421-7_2

Prabhu, S. D., & Frangogiannis, N. G. (2016). The Biological Basis for Cardiac Repair After Myocardial Infarction: From Inflammation to Fibrosis. *Circulation Research*, *119*(1), 91–112. https://doi.org/10.1161/CIRCRESAHA.116.303577

Prato, F. S., Butler, J., Sykes, J., Keenliside, L., Blackwood, K. J., Thompson, R. T., White, J. A., Mikami, Y., Thiessen, J. D., & Wisenberg, G. (2015). Can The Inflammatory Response Be Evaluated Using 18F-FDG Within Zones of Microvascular Obstruction Following Myocardial Infarction? *Journal of Nuclear Medicine*, *56*(2), 299–304. https://doi.org/10.2967/JNUMED.114.147835

Pullen, A. B., Kain, V., Serhan, C. N., & Halade, G. v. (2020). Molecular and cellular differences in cardiac repair of male and female mice. *Journal of the American Heart Association*, *9*(8). https://doi.org/10.1161/JAHA.119.015672

Pupkaite, J., Sedlakova, V., Eren Cimenci, C., Bak, M., McLaughlin, S., Ruel, M., Alarcon, E. I., & Suuronen, E. J. (2020). Delivering More of an Injectable Human Recombinant Collagen III Hydrogel Does Not Improve Its Therapeutic Efficacy for Treating Myocardial Infarction. *ACS Biomaterials Science and Engineering*, *6*(7), 4256–4265. https://doi.org/10.1021/ACSBIOMATERIALS.0C00418/SUPPL_FILE/AB0C00418_SI_001.PDF

Pytliak, M., Vaník, V., & Bojčík, P. (2017). Heart Remodelation: Role of MMPs. *The Role of Matrix Metalloproteinase in Human Body Pathologies*. https://doi.org/10.5772/INTECHOPEN.71662

Quillard, T., Croce, K., Jaffer, F. A., Weissleder, R., & Libby, P. (2011). Molecular imaging of macrophage protease activity in cardiovascular inflammation in vivo. *Thrombosis and Haemostasis*, *105*(5), 828. https://doi.org/10.1160/TH10-09-0589

Ra, H. J., & Parks, W. C. (2007). Control of Matrix Metalloproteinase Catalytic Activity. *Matrix Biology : Journal of the International Society for Matrix Biology*, *26*(8), 587. https://doi.org/10.1016/J.MATBIO.2007.07.001

Raeeszadeh-Sarmazdeh, M., Do, L. D., & Hritz, B. G. (2020). Metalloproteinases and Their Inhibitors: Potential for the Development of New Therapeutics. *Cells 2020, Vol. 9, Page 1313*, *9*(5), 1313. https://doi.org/10.3390/CELLS9051313

Rangasamy, L., di Geronimo, B., Ortín, I., Coderch, C., Zapico, J. M., Ramos, A., & de Pascual-Teresa, B. (2019). Molecular Imaging Probes Based on Matrix Metalloproteinase Inhibitors (MMPIs). *Molecules (Basel, Switzerland)*, *24*(16). https://doi.org/10.3390/MOLECULES24162982

Richardson, W. J., Clarke, S. A., Alexander Quinn, T., & Holmes, J. W. (2015). Physiological Implications of Myocardial Scar Structure. *Comprehensive Physiology*, *5*(4), 1877–1909. https://doi.org/10.1002/CPHY.C140067

Rienks, M., Papageorgiou, A. P., Frangogiannis, N. G., & Heymans, S. (2014). Myocardial extracellular matrix: an ever-changing and diverse entity. *Circulation Research*, *114*(5), 872–888. https://doi.org/10.1161/CIRCRESAHA.114.302533

Rowe, S. P., & Pomper, M. G. (2021). Molecular imaging in oncology: Current impact and future directions. *CA: A Cancer Journal for Clinicians*. https://doi.org/10.3322/CAAC.21713

Sahul, Z. H., Mukherjee, R., Song, J., McAteer, J., Stroud, R. E., Dione, D. P., Staib, L., Papademetris, X., Dobrucki, L. W., Duncan, J. S., Spinale, F. G., & Sinusas, A. J. (2011). Targeted imaging of the spatial and temporal variation of matrix metalloproteinase activity in a porcine model of postinfarct remodeling: relationship to myocardial dysfunction. *Circulation. Cardiovascular Imaging*, *4*(4), 381–391. https://doi.org/10.1161/CIRCIMAGING.110.961854

Saleh, M., & Ambrose, J. A. (2018). Understanding myocardial infarction. *F1000Research*, *7*. https://doi.org/10.12688/F1000RESEARCH.15096.1

Saraste, A., Ståhle, M., & Roivainen, A. (2020). Evaluation of cardiac function by nuclear imaging in preclinical studies. *Journal of Nuclear Cardiology : Official Publication of the American Society of Nuclear Cardiology*, *27*(4), 1328–1330. https://doi.org/10.1007/S12350-019-01784-Y

Schellenberger, E., Rudloff, F., Warmuth, C., Taupitz, M., Hamm, B., & Schnorr, J. (2008). Protease-specific nanosensors for magnetic resonance imaging. *Bioconjugate Chemistry*, *19*(12), 2440–2445. https://doi.org/10.1021/BC800330K

Schirone, L., Forte, M., Palmerio, S., Yee, D., Nocella, C., Angelini, F., Pagano, F., Schiavon, S., Bordin, A., Carrizzo, A., Vecchione, C., Valenti, V., Chimenti, I., Falco, E. de, Sciarretta, S., & Frati, G. (2017). A Review of the Molecular Mechanisms Underlying the Development and Progression of Cardiac Remodeling. *Oxidative Medicine and Cellular Longevity*, *2017*. https://doi.org/10.1155/2017/3920195

Souders, C. A., Bowers, S. L. K., & Baudino, T. A. (2009). Cardiac Fibroblast: The Renaissance Cell. *Circulation Research*, *105*(12), 1164. https://doi.org/10.1161/CIRCRESAHA.109.209809

Soufen, H. N., Salemi, V. M. C., Aneas, I. M. S., Ramires, F. J. A., Benício, A. M. D., Benvenuti, L. A., Krieger, J. E., & Mady, C. (2008). Collagen content, but not the ratios of collagen type III/I mRNAs, differs among hypertensive, alcoholic, and idiopathic dilated cardiomyopathy. *Brazilian Journal of Medical and Biological Research*, *41*(12), 1098–1104. https://doi.org/10.1590/S0100-879X2008001200009

st. John Sutton, M. G., & Sharpe, N. (2000). Left ventricular remodeling after myocardial infarction: pathophysiology and therapy. *Circulation*, *101*(25), 2981–2988. https://doi.org/10.1161/01.CIR.101.25.2981

Stewart, S., MacIntyre, K., Capewell, S., & McMurray, J. J. V. (2003). Heart failure and the aging population: an increasing burden in the 21st century? *Heart (British Cardiac Society)*, *89*(1), 49–53. https://doi.org/10.1136/HEART.89.1.49

Su, H., Spinale, F. G., Dobrucki, L. W., Song, J., Hua, J., Sweterlitsch, S., Dione, D. P., Cavaliere, P., Chow, C., Bourke, B. N., Hu, X. Y., Azure, M., Yalamanchili, P., Liu, R., Cheesman, E. H., Robinson, S., Edwards, D. S., & Sinusas, A. J. (2005). Noninvasive targeted imaging of matrix metalloproteinase activation in a murine model of postinfarction remodeling. *Circulation*, *112*(20), 3157–3167. https://doi.org/10.1161/CIRCULATIONAHA.105.583021

Takagawa, J., Zhang, Y., Wong, M. L., Sievers, R. E., Kapasi, N. K., Wang, Y., Yeghiazarians, Y., Lee, R. J., Grossman, W., & Springer, M. L. (2007). Myocardial infarct size measurement in the mouse chronic infarction model: comparison of area- and length-

based approaches. *Journal of Applied Physiology (Bethesda, Md. : 1985)*, *102*(6), 2104–2111. https://doi.org/10.1152/JAPPLPHYSIOL.00033.2007

Talman, V., & Ruskoaho, H. (2016). Cardiac fibrosis in myocardial infarction—from repair and remodeling to regeneration. *Cell and Tissue Research*, *365*(3), 563. https://doi.org/10.1007/S00441-016-2431-9

Tao, Z. Y., Cavasin, M. A., Yang, F., Liu, Y. H., & Yang, X. P. (2004). Temporal changes in matrix metalloproteinase expression and inflammatory response associated with cardiac rupture after myocardial infarction in mice. *Life Sciences*, *74*(12), 1561–1572. https://doi.org/10.1016/J.LFS.2003.09.042

Thiene, G., & Basso, C. (2010). Myocardial infarction: a paradigm of success in modern medicine. *Cardiovascular Pathology : The Official Journal of the Society for Cardiovascular Pathology*, *19*(1), 1–5. https://doi.org/10.1016/J.CARPATH.2009.08.002

Thorn, S. L., Barlow, S. C., Feher, A., Stacy, M. R., Doviak, H., Jacobs, J., Zellars, K., Renaud, J. M., Klein, R., deKemp, R. A., Khakoo, A. Y., Lee, T. W., Spinale, F. G., & Sinusas, A. J. (2019). Application of Hybrid Matrix Metalloproteinase-Targeted and Dynamic 201Tl Single-Photon Emission Computed Tomography/Computed Tomography Imaging for Evaluation of Early Post-Myocardial Infarction Remodeling. *Circulation. Cardiovascular Imaging*, *12*(11), e009055. https://doi.org/10.1161/CIRCIMAGING.119.009055

Turner, P. v., Brabb, T., Pekow, C., & Vasbinder, M. A. (2011). Administration of Substances to Laboratory Animals: Routes of Administration and Factors to Consider. *Journal of the American Association for Laboratory Animal Science : JAALAS*, *50*(5), 600. /pmc/articles/PMC3189662/

van de Wiele, C., & Oltenfreiter, R. (2006). Imaging probes targeting matrix metalloproteinases. *Cancer Biotherapy & Radiopharmaceuticals*, *21*(5), 409–417. https://doi.org/10.1089/CBR.2006.21.409

van der Bijl, P., Abou, R., Goedemans, L., Gersh, B. J., Holmes, D. R., Ajmone Marsan, N., Delgado, V., & Bax, J. J. (2020). Left Ventricular Post-Infarct Remodeling: Implications for Systolic Function Improvement and Outcomes in the Modern Era. *JACC. Heart Failure*, *8*(2), 131–140. https://doi.org/10.1016/J.JCHF.2019.08.014

Vanhoutte, D., Schellings, M., Pinto, Y., & Heymans, S. (2006). Relevance of matrix metalloproteinases and their inhibitors after myocardial infarction: a temporal and spatial window. *Cardiovascular Research*, *69*(3), 604–613. https://doi.org/10.1016/J.CARDIORES.2005.10.002

Vazquez, N., Missault, S., Vangestel, C., Deleye, S., Thomae, D., van der Veken, P., Augustyns, K., Staelens, S., Dedeurwaerdere, S., & wyffels, L. (2017). Evaluation of [18 F]BR420 and [18 F]BR351 as radiotracers for MMP-9 imaging in colorectal cancer. *Journal of Labelled Compounds & Radiopharmaceuticals*, *60*(1), 69–79. https://doi.org/10.1002/JLCR.3476

Vilahur, G., Juan-Babot, O., Peña, E., Oñate, B., Casaní, L., & Badimon, L. (2011). Molecular and cellular mechanisms involved in cardiac remodeling after acute myocardial infarction. *Journal of Molecular and Cellular Cardiology*, *50*(3), 522–533. https://doi.org/10.1016/J.YJMCC.2010.12.021

Wagner, S., Faust, A., Breyholz, H. J., Schober, O., Schäfers, M., & Kopka, K. (2011). The MMP inhibitor (R)-2-(N-benzyl-4-(2-[18F]fluoroethoxy)phenylsulphonamido)-N-hydroxy-3-methylbutanamide: Improved precursor synthesis and fully automated radiosynthesis. *Applied Radiation and Isotopes : Including Data, Instrumentation and*

Methods for Use in Agriculture, Industry and Medicine, *69*(6), 862–868. https://doi.org/10.1016/J.APRADISO.2011.02.038

Wilk, B., Wisenberg, G., Dharmakumar, R., Thiessen, J. D., Goldhawk, D. E., & Prato, F. S. (2019). Hybrid PET/MR imaging in myocardial inflammation post-myocardial infarction. *Journal of Nuclear Cardiology 2019 27:6*, *27*(6), 2083–2099. https://doi.org/10.1007/S12350-019-01973-9

Wilson, E. M., Moainie, S. L., Baskin, J. M., Lowry, A. S., Deschamps, A. M., Mukheljee, R., Guy, T. S., st. John-Sutton, M. G., Gorman, J. H., Edmunds, L. H., Gorman, R. C., & Spinale, F. G. (2003). Region- and type-specific induction of matrix metalloproteinases in post-myocardial infarction remodeling. *Circulation*, *107*(22), 2857–2863. https://doi.org/10.1161/01.CIR.0000068375.40887.FA

Wu, E., Ortiz, J. T., Tejedor, P., Lee, D. C., Bucciarelli-Ducci, C., Kansal, P., Carr, J. C., Holly, T. A., Lloyd-Jones, D., Klocke, F. J., & Bonow, R. O. (2008). Infarct size by contrast enhanced cardiac magnetic resonance is a stronger predictor of outcomes than left ventricular ejection fraction or end-systolic volume index: prospective cohort study. *Heart (British Cardiac Society)*, *94*(6), 730–736. https://doi.org/10.1136/HRT.2007.122622

Xue, M., & Jackson, C. J. (2015). Extracellular Matrix Reorganization During Wound Healing and Its Impact on Abnormal Scarring. *Advances in Wound Care*, *4*(3), 119. https://doi.org/10.1089/WOUND.2013.0485

Yang, F., Liu, Y. H., Yang, X. P., Xu, J., Kapke, A., & Carretero, O. A. (2002). Myocardial infarction and cardiac remodelling in mice. *Experimental Physiology*, *87*(5), 547–555. https://doi.org/10.1113/EPH8702385

Zhang, H., & Faber, J. E. (2015). De-novo Collateral Formation Following Acute Myocardial Infarction: Dependence on CCR2+ Bone Marrow Cells. *Journal of Molecular and Cellular Cardiology*, *87*, 4. https://doi.org/10.1016/J.YJMCC.2015.07.020

Zhang, Y., Thorn, S., DaSilva, J. N., Lamoureux, M., DeKemp, R. A., Beanlands, R. S., Ruel, M., & Suuronen, E. J. (2008). Collagen-based matrices improve the delivery of transplanted circulating progenitor cells: development and demonstration by ex vivo radionuclide cell labeling and in vivo tracking with positron-emission tomography. *Circulation. Cardiovascular Imaging*, *1*(3), 197–204. https://doi.org/10.1161/CIRCIMAGING.108.781120

Zhong, M., Alonso, C. E., Taegtmeyer, H., & Kundu, B. K. (2013). Quantitative PET imaging detects early metabolic remodeling in a mouse model of pressure-overload left ventricular hypertrophy in vivo. *Journal of Nuclear Medicine : Official Publication, Society of Nuclear Medicine*, *54*(4), 609–615. https://doi.org/10.2967/JNUMED.112.108092

Zinnhardt, B., Pigeon, H., Thézé, B., Viel, T., Wachsmuth, L., Fricke, I. B., Schelhaas, S., Honold, L., Schwegmann, K., Wagner, S., Faust, A., Faber, C., Kuhlmann, M. T., Hermann, S., Schäfers, M., Winkeler, A., & Jacobs, A. H. (2017). Combined PET Imaging of the Inflammatory Tumor Microenvironment Identifies Margins of Unique Radiotracer Uptake. *Cancer Research*, *77*(8), 1831–1841. https://doi.org/10.1158/0008-5472.CAN-16-2628

Zinnhardt, B., Viel, T., Wachsmuth, L., Vrachimis, A., Wagner, S., Breyholz, H. J., Faust, A., Hermann, S., Kopka, K., Faber, C., Dollé, F., Pappata, S., Planas, A. M., Tavitian, B., Schäfers, M., Sorokin, L. M., Kuhlmann, M. T., & Jacobs, A. H. (2015). Multimodal

imaging reveals temporal and spatial microglia and matrix metalloproteinase activity after experimental stroke. *Journal of Cerebral Blood Flow and Metabolism : Official Journal of the International Society of Cerebral Blood Flow and Metabolism*, *35*(11), 1711–1721. https://doi.org/10.1038/JCBFM.2015.149